REPORT DOCUMENTATION PAGE

AFRL-SR-AR-TR-03-

0219

Public reporting burden for this collection of information is estimated to average 1 hour per response, including the time for reviewing instru data needed, and completing and reviewing this collection of information. Send comments regarding this burden estimate or any other asp this burden to Department of Defense, Washington Headquarters Services, Directorate for Information Operations and Reports (0704-018 4302. Respondents should be aware that notwithstanding any other provision of law, no person shall be subject to any penalty for failing to valid OMB control number. PLEASE DO NOT RETURN YOUR FORM TO THE ABOVE ADDRESS.

1. REPORT DATE (DD-MM-YYYY) 5/4/2003	2. REPORT TYPE Final Technical Report	3. DATES COVERED (From - To) 12/2000-3/2003
4. TITLE AND SUBTITLE Parallel Multigrid DNS/LES Methods for Time-Dependent Turbulent Flow		5a. CONTRACT NUMBER
		5b. GRANT NUMBER F49620-01-1-0028
		5c. PROGRAM ELEMENT NUMBER
6. AUTHOR(S) Chaoqun Liu, Professor & Director		5d. PROJECT NUMBER
		5e. TASK NUMBER
		5f. WORK UNIT NUMBER
7. PERFORMING ORGANIZATION NAME(S) AND ADDRESS(ES) Univ. of Texas at Arlington Dept. of Mathematics Center for Numerical Simulation & Modeling Arlington, TX 76019		8. PERFORMING ORGANIZATION REPORT NUMBER
9. SPONSORING / MONITORING AGENCY NAME(S) AND ADDRESS(ES) Dr. Tom Beutner AFOSR/NA 4015 Wilson Blvd., #713 Arlington, VA 22203		10. SPONSOR/MONITOR'S ACRONYM(S)
		11. SPONSOR/MONITOR'S REPORT NUMBER(S)

12. DISTRIBUTION / AVAILABILITY STATEMENT No restriction

DISTRIBUTION STATEMENT A
Approved for Public Release
Distribution Unlimited

20030623 015

13. SUPPLEMENTARY NOTES None

14. ABSTRACT

During the past two years (12/00-3/03), we have developed a very efficient and reliable direct numerical simulation (DNS) and large eddy simulation (LES) software (DNSUTA) for compressible flow in a curvilinear coordinates which is a continuation of our previous effort supported by AFOSR. The software includes a high-quality grid generation code which can generate smooth and near-orthogonal, body-fitted grids and a parallel efficient flow solver which applies sixth-order compact scheme, eighth-order filter, LU-SGS flow solver, non-reflecting boundary condition, high-order weighted compact scheme for shock capturing, structure function sub-grid model, and MPI parallel computation. The code has been successfully used for prediction of flow transition around flat plate and airfoils with various attack angles. The code has also been used for flow separation control for low Reynolds airfoils with steady and pulsed blowing jets. All of these simulations are real time dependent, 3-D, with general geometry and have demonstrated qualitative or quantitative agreement with experiment or theoretical work. We believe the topics described above are very challenging and our accomplishment is very significant for both basic science and Air Force mission. The high-order weighted compact scheme and non-reflecting boundary conditions in a curvilinear coordinate are the original work conducted by us which is a significant contribution to the CFD community.

15. SUBJECT TERMS

16. SECURITY CLASSIFICATION OF: unclassified			17. LIMITATION OF ABSTRACT None	18. NUMBER OF PAGES 61	19a. NAME OF RESPONSIBLE PERSON Chaoqun Liu
a. REPORT X	b. ABSTRACT	c. THIS PAGE			19b. TELEPHONE NUMBER (include area code) 817-272-5151

Standard Form 298 (Rev. 8-98)
Prescribed by ANSI Std. Z39.18
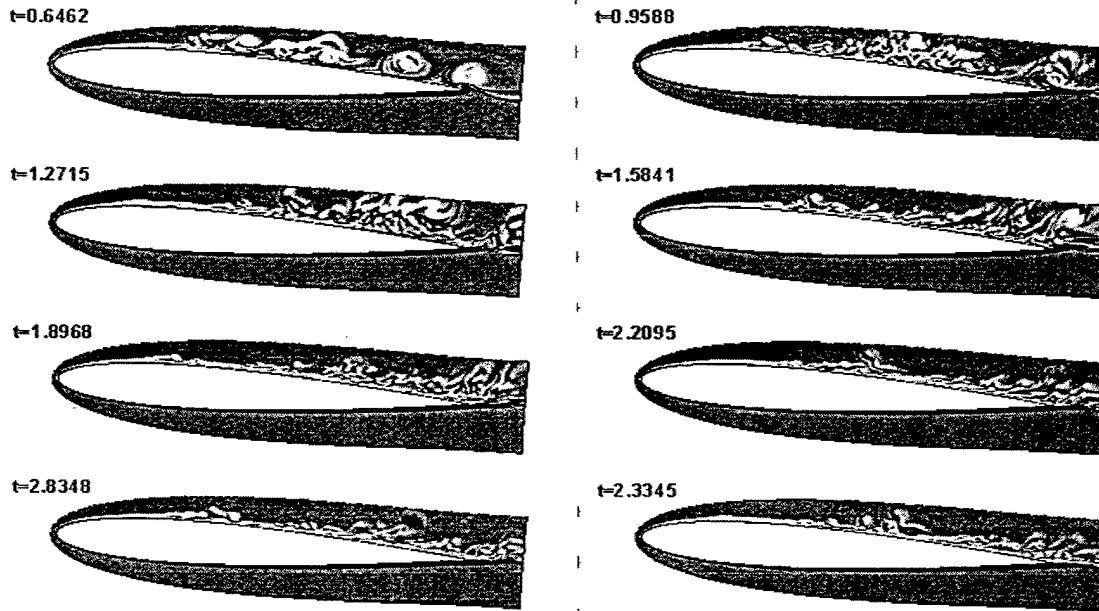
FINAL TECHNICAL REPORT

Parallel Multigrid DNS/LES Methods for Time-Dependent Compressible Turbulent Flow

t=0.6462 t=0.9588 t=1.2715 t=1.5841 t=1.8968 t=2.2095 t=2.8348 t=2.3345

Principal Investigator:

Dr. Chaoqun Liu
Professor & Director
Center for Numerical Simulation
and Modeling
Department of Mathematics
University of Texas at Arlington
Arlington, TX 76019
Phone: (817) 272-5151
E-Mail: cliu@uta.edu

Program Manager:

Dr. Tom Beutner
Program Manager
AFOSR/NA
4015 Wilson Blvd.
Room 713
Arlington, VA 22203
Phone : (703) 696-6961
E-Mail tom.beutner@afosr.af.mil

May 1, 2003

Table Contents

ABSTRACT

During the past two years (12/00-3/03), we have developed a very efficient and reliable direct numerical simulation (DNS) and large eddy simulation (LES) software (DNSUTA) for compressible flow in a curvilinear coordinates which is a continuation of our previous effort supported by AFOSR. The software includes a high-quality grid generation code which can generate smooth and near-orthogonal, body-fitted grids and a parallel efficient flow solver which applies sixth-order compact scheme, eighth-order filter, LU-SGS flow solver, non-reflecting boundary condition, high-order weighted compact scheme for shock capturing, structure function sub-grid model, and MPI parallel computation. The code has been successfully used for prediction of flow transition around flat plate and airfoils with various attack angles. The code has also been used for flow separation control for low Reynolds airfoils with steady and pulsed blowing jets. All of these simulations are real time dependent, 3-D, with general geometry and have demonstrated qualitative or quantitative agreement with experiment or theoretical work. We believe the topics described above are very challenging and our accomplishment is very significant for both basic science and Air Force mission. The high-order weighted compact scheme and non-reflecting boundary conditions in a curvilinear coordinate are the original work conducted by us which is a significant contribution to the CFD community.

The code is currently used by NASA Langley for prediction of flow transition and turbulence through a technology transfer contract. The code has passed all NASA test cases and demonstrated its high accuracy and high reliability. The code and related work have been recognized by NASA Langley Researchers as unique in the United States. The code also attracts significant interests from US Navy for study of wakes and propeller flows.

Because of the unexpected notice issued by AFOSR that the Optional 2 of our grant will not be exercised due to funding restrictions, we lost the optional fund for the third year and, therefore, we did not have enough time to complete all of work we proposed.

Chapter 1

Introduction

Turbulent flow prediction and analysis are very important to Air Force missions. There are, in general, three ways to conduct turbulent flow prediction - direct numerical simulation (DNS), large eddy simulation (LES), and Reynolds averaged Navier-Stokes solver (RANS), while the time-dependent Navier-Stokes equations are still widely accepted as a governing system for both laminar and turbulent flows.

The classical averaging method is so-called Reynolds averaging which appeared around one hundred years ago and is still widely used by industry. RANS is an economic way to simulate turbulent flow assuming a mean flow followed by a perturbation. RANS only studies the flow mean value. However, in many important flow-related topics including boundary layer receptivity, flow transition, flow separation, wakes, interaction of flow separation and wakes, noise generation, vortex dynamics, flow-structure interaction, unsteady turbulence, turbulent heat transfer, hypersonic chemically reacting flow, shock-turbulent boundary layer interaction, suppression of turbulence, etc., which Air Force is highly interested in, only the instantaneous quantities are critical. For these Air Force interests, DNS or, at least, LES must be used. Although DNS is very expensive, there is still a large demand for developing efficient DNS technology.

The RANS system is not self-closed and many correlation terms need to be modeled. Most popular eddy viscosity models assume Reynolds stress is proportional to strain of the mean flow. Unfortunately, modern fluid mechanics study has found there is no such a correlation. The interaction between large length scales and small length scales is very complicated. Most early turbulence models assume the turbulence is isotropic, an assumption that is now understood to be unrealistic especially for wall-bounded flow. Some new turbulence models, like Reynolds stress models, have been offered in attempts to remove the assumption, but these models introduce higher-order closure problems. RANS is currently used widely by industry and is expected to be relied upon until we have new reliable and feasible approaches. However, RANS has fundamental limitations and deficiencies. Turbulence models are usually empirical and case-related. In general, they are good for some cases largely because of adjustment of coefficients, but not accurate for other cases. It is really hard or almost impossible to find a universal model which can predict well for all flow cases. As pointed out by AGARD-CP-551 at its Foreword, "one of the main conclusions was that no one model, or type of model, could predict all the test cases to good engineering accuracy. The implication of this result is that for certain cases Large Eddy Simulation or Direct Numerical Simulation may be the only recourse for obtaining an accurate prediction" (AGARD, 1994).

Then, we have to look back to the original time-dependent Navier-Stokes equations in our search for solutions. This leads us to direct numerical simulation (DNS). DNS is the only numerical approach dealing with the exact solution of 3-D time-dependent N-S equations without any ad hoc assumption and in which leads all cases to good engineering accuracy. However, it is still too expensive if we want to resolve all length scales including the Kolmogorov scale especially for high Reynolds number and general

geometries. We need to refine the grids in certain areas where the small length scale is important. More realistic at present time is to look for some compromise which resolves most significant large vortex and leave small length scales (smaller than the grid size) for modeling. This will lead to large eddy simulation (LES). In LES, the time- and space-dependent large scales will be simulated and models are only needed for scales smaller than the grid size. Although the small length scales are more dissipative and easier to model, the grid size must be relatively small until the subgird scale is less important in LES in order to achieve accurate results.

DNS for flows with low Reynolds number and simple geometry has been successfully performed and it is widely recognized that DNS can help understand flow physics and can check and improve turbulence models. The question is whether or not, in any sense, DNS can work for real world. The fundamental problem with DNS/LES seems to be solved and our experience shows DNS can be used for flow transition and LES can be used for fully developed turbulent flow for a spectrum of engineering applications.

The recent developments in computer performance and numerical algorithms seem to bring hope to the DNS/LES community that DNS/LES can in the near future be modified for high Reynolds numbers and complex geometries. There are several hopeful signs: First, computer capability has increased dramatically every year. The new generation of parallel machines with 1000 processors and distributed memory can have Terra-bytes of memory. The price of memory has dropped sharply. The problem with computer memory requirements seems to be gradually disappearing. The CPU capacity remains a challenge. The fastest parallel machine with 1000 processors nowadays can perform over two Terra-flop, raising by one order the Reynolds numbers that can be covered. Nowadays, at least 200 millions of grids can be used for flow simulation on currently available supercomputers. More recently, Linux PC-Cluster has been well developed and widely used which reduces the computer cost by one order to the range of $20-30k for 16 CPUs, which is affordable to most aerospace companies and encourages more scientists and engineers to use DNS/LES for flow simulations. Second, DNS for complex geometry is feasible. It requires a high-order grid generation, high grid quality and, moreover, high order discretization and high order filter for general curvilinear coordinates. A typical turbulent flow has a transition process which includes receptivity of environmental disturbances, linear growth, nonlinear instability, breakdowns, and transition, eventually, to a fully developed turbulent flow. The length scale changes at every stage. In the main flow, the length scale can be thought of as $O(1)$. In general, the receptivity and early transition processes are dominated by large scales of the order of $O(\mathrm{Re})^{-\frac{1}{2}}$. At these stages the grid size need not to be very small. Probably it is small enough if it can resolve the Tollmien-Schlichting waves. Therefore, DNS can be used for main flow and early transition stages for some realistic Reynolds numbers and realistic geometries. When the flow enters the non-linear transition zone and finally becomes fully developed turbulent flow, the smallest length scale may reach $O(\mathrm{Re})^{-\frac{3}{4}}$. When the Reynolds number is very high, we still do not have enough grids to resolve them. We can only resolve those scales greater than or equal to the grid size and have to model other flows with high Reynolds number and general geometries. DNS/LES for complex geometry was criticized, but now an increasing number of researchers (e.g. Liu, et al, 1994, 1998a, 1998b; Jiang, 1999a,

2001b; Shan 2000a, 2000b; Visbal et al., 1998; Adams, 2000; Rizzettz et al, 2001; etc.) are working on this direction. Nowadays, DNS/LES can capture the major feature of transitional and turbulent flow around a 3-D airfoil based on the currently available parallel computers.

Looking around for the trend of CFD, we can find more and more scientists have realized the problem with the Reynolds averaging and focused their research on DNS or LES. The time has come to orient numerical simulation to the real world. The "real world" for flows around flight vehicles has the following features:

(1) The flow is real-time dependent,

(2) The vehicles are geometrically very complex,

(3) The vehicles operate at Mach numbers which range from high subsonic through high supersonic, or even hypersonic in the near future, where finite-rate chemical reactions must be considered,

(4) The flow field is a combination of laminar flow, transitional flow, and fully developed turbulent flow.

It is understood that the following challenges for DNS/LES of turbulent flows should be met:

(1) High-order accuracy discretization in both time and space in a curvilinear coordinate.

(2) High-order shock-capturing for transonic and supersonic flows.

(3) High-order grid generation and grid mapping for general configurations.

(4) Very fine resolution for boundary layers, especially the near-wall region, to resolve small-scale eddies involved in the transition process and turbulence.

(5) High-order filters and reliable subgrid scale models.

(6) High code efficiency to reduce CPU cost to a reasonable level.

These are very challenging requirements. However, our approach has, in principle, provided a solid base to meet the above requirements and is therefore a feasible approach to DNS/LES for engineering applications.

The serious problem is that the small length scales will become important when the flow enters the late transition stage (non-linear and breakdown stages). In the case that the Reynolds number is high and geometry is complicated where our grid resource still cannot provide enough resolution, we can then use LES. Therefore, we can say that based on the capability of current available supercomputers, we can use DNS/LES to solve turbulent flow in turbomachinery which has a Reynolds number of around 10^5. The DNS can be also used for 3-D airfoil flow transition for a Reynolds number of around $10^5 - 10^6$. The Reynolds number can be near one order higher if we use subgrid models (LES).

Our work has considered both the basic science advances and the Air Force needs. It is therefore anticipated that the success of our NDS/LES code will provide the following potential to AFOSR and other federal agencies (NASA, ONR, etc):

(1) Provide a detailed description of the whole process of boundary layer receptivity, flow separation, wakes, interaction of flow separation and wakes, noise generation, vortex dynamics, shock-turbulent boundary interaction, suppression of turbulence, flow transition and turbulence structure. This will have a notable impact on fundamental fluid mechanics.

(2) Help understand the origin of turbulence such as how the environmental disturbance in free stream induces unstable wave modes in boundary layers and what causes the non-linear instability and flow breakdown and how the unstable wakes induce the original inviscid shear layer instability for airfoils with attack angle (see Jiang et al, 2003).

(3) Provide a "Computational Wind Tunnel" which can give a full simulation of turbulent flow around airfoils for flow transition, separation, and flow control.

(4) Provide assistance to transition control, drag reduction, noise reduction, and improvement of aircraft design. As advances are made in supercomputer performance DNS/LES for engineering design will become feasible with more complex geometry and high-Reynolds number. It will provide a right answer to flow prediction on drag and heat transfer.

During the past two years, 12/00-3/03, we have successfully developed a very accurate and reliable DNS/LES code (DBNSUTA). The code has been successfully used to simulate the whole process of flow transition for flat plate and airfoils at both low speed ($M_\infty = 0.2$ for flat plate and airfoils) and high speed (flat plate at $M_\infty = 4.5$). The DNS and LES results have been well documented and validated (see Liu et al, 1991a, 1991b, 1993, 1994a, 1994b, 1995, 1998a, 1998b; Shan et al, 1999a, 1999b, 1999c, 2000a, 200b; Jiang et al, 199a, 199b, 2001a, 2001b, 2003;).

The code has been validated by the authors in a number of publications and by NASA users. NASA Langley personnel (Choudahari et al, 2003a and 2003b) used DNSUTA for a number of cases of flow transition including flat plate, swept wing and straight cone and found the validation is very satisfactory. The code also attracts significant interests to US Navy for study of wakes and propeller flows. As a Navy David Taylor researcher points out (personal communication), we have no sense to wait for 5 years for developing LES code for general geometry, but not to use 'DNSUTA' to simulate wakes now.

Recently, Dr. Liu and his colleague have use DNSUTA to successfully simulate the flow separation and transition around airfoil NACA0012 with four degree of attack angle and Reynolds number of 100,000. They also use DNSUTA for flow control with pulsed and screwed blowing jets. These achievements clearly show the purpose of this project has been achieved successfully. Unfortunately, we cannot complete all tasks we proposed due to the sudden stop of Option 2 fund noticed by AFOSR contracting office. We lost Optional 2 fund for the third year and then do not have enough time to complete all work we proposed.

Chapter 2

Our Technical Approaches

Our DNS/LES code adopts state of art approaches including orthogonal grid generation, high-order Jacobien in curvilinear coordinates, high-order compact scheme, high-order filter (filtering the LES solution at each time step), high-order weighted compact scheme, non-reflecting boundary condition, efficient Navier-Stokes solver, effective dynamic sub-grid model, and parallel computation. The high-order weighted compact scheme is particularly critical, which can capture the shock very accurately and keep high-order for smooth areas. The effectiveness of the subgrid model is another critical factor that would ensure the accuracy of LES with rather coarse grids. Our work on weighted compact scheme and non-reflecting boundary condition in a curvilinear coordinate are original and are a significant contribution to the CFD community.

2.1 Contravariant velocity-based governing equations:

The three-dimensional time-dependent Navier-Stokes equations in generalized curvilinear coordinates (ξ, η, ζ) can be written in conservative forms:

$$\frac{1}{J}\frac{\partial Q}{\partial t} + \frac{\partial (E - E_v)}{\partial \xi} + \frac{\partial (F - F_v)}{\partial \eta} + \frac{\partial (F - F_v)}{\partial \zeta} = 0 \qquad (2.1)$$

The vector of conserved quantities Q, inviscid flux vector (E, F, G), and viscous flux vector (E_v, F_v, G_v) are defined via

$$Q = \begin{pmatrix} \rho \\ \rho u \\ \rho v \\ \rho w \\ e \end{pmatrix}, \quad E = \frac{1}{J}\begin{pmatrix} \rho U \\ \rho U u + p\xi_x \\ \rho U v + p\xi_y \\ \rho U w + p\xi_z \\ U(e+p) \end{pmatrix}, \quad F = \frac{1}{J}\begin{pmatrix} \rho V \\ \rho V u + p\eta_x \\ \rho V v + p\eta_y \\ \rho V w + p\eta_z \\ V(e+p) \end{pmatrix}, \quad G = \frac{1}{J}\begin{pmatrix} \rho W \\ \rho W u + p\zeta_x \\ \rho W v + p\zeta_y \\ \rho W w + p\zeta_z \\ W(e+p) \end{pmatrix},$$

$$E_v = \frac{1}{J}\begin{pmatrix} 0 \\ \tau_{xx}\xi_x + \tau_{yx}\xi_y + \tau_{zx}\xi_z \\ \tau_{xy}\xi_x + \tau_{yy}\xi_y + \tau_{zy}\xi_z \\ \tau_{xz}\xi_x + \tau_{yz}\xi_y + \tau_{zz}\xi_z \\ q_x\xi_x + q_y\xi_y + q_z\xi_z \end{pmatrix}, \qquad F_v = \frac{1}{J}\begin{pmatrix} 0 \\ \tau_{xx}\eta_x + \tau_{yx}\eta_y + \tau_{zx}\eta_z \\ \tau_{xy}\eta_x + \tau_{yy}\eta_y + \tau_{zy}\eta_z \\ \tau_{xz}\eta_x + \tau_{yz}\eta_y + \tau_{zz}\eta_z \\ q_x\eta_x + q_y\eta_y + q_z\eta_z \end{pmatrix},$$

$$G_v = \frac{1}{J}\begin{pmatrix} 0 \\ \tau_{xx}\zeta_x + \tau_{yx}\zeta_y + \tau_{zx}\zeta_z \\ \tau_{xy}\zeta_x + \tau_{yy}\zeta_y + \tau_{zy}\zeta_z \\ \tau_{xz}\zeta_x + \tau_{yz}\zeta_y + \tau_{zz}\zeta_z \\ q_x\zeta_x + q_y\zeta_y + q_z\zeta_z \end{pmatrix}$$

where $J = \dfrac{\partial(\xi,\eta,\zeta)}{\partial(x,y,z)}$ is Jacobian of the coordinate transformation between the curvilinear (ξ,η,ζ) and Cartesian (x,y,z) frames, and $\xi_x, \xi_y, \xi_z, \eta_x, \eta_y, \eta_z, \zeta_x, \zeta_y, \zeta_z$ are coordinate transformation metrics. The contravariant velocity components U, V, W are defined as

$$U \equiv u\xi_x + v\xi_y + w\xi_z, \ V \equiv u\eta_x + v\eta_y + w\eta_z, \ W \equiv u\zeta_x + v\zeta_y + w\zeta_z,$$

$$e = \frac{p}{\gamma - 1} + \frac{1}{2}\rho(u^2 + v^2 + w^2).$$

The components of the viscous stress tensor are denoted by $\tau_{xx}, \tau_{yy}, \tau_{zz}, \tau_{xy}, \tau_{xz}, \tau_{yz}$. The density, velocity components and pressure are defined by ρ, u, v, w and p.

2.2 Orthogonal grid generation and high order Jacobian

In order to achieve high-order accuracy, say fourth-order or higher, first, a high-order description of Jacobian metrics, e.g., ξ_x, ξ_y, etc. is required. Second, the high quality of grids, i.e. continuity in curvature must be guaranteed. Note that there are several Jacobian grid mapping terms, J, ξ_x, ξ_y, … in our governing equations which need to be evaluated by a high-order finite difference scheme to guarantee the accuracy of our high-order discretization. As shown by numerical experiment, any discontinuity or disturbance in surface curvature will result in a totally different output with same inflow disturbance. Accurate LES requires a very smooth gird generation where the second-order derivative is continuous and the third-order derivative exists everywhere. Also an orthogonal grid especially near the solid surface is preferred. A high-quality elliptic grid generation has been carried out for 2-D airfoil and 3-D Delta wing (Shan et al, 2000, Figure 1 and 2). An elliptic grid generation method, first proposed by Spekreijse (1995), is used to construct the three-dimensional grids. This method is based on a composite mapping, which consists of a nonlinear transfinite algebraic transformation and an elliptic transformation. The grids are orthogonal on the delta wing surface. The three-dimensional grid sketch can be found in Figure 2 which shows we have generated smooth and near orthogonal high-quality grids.
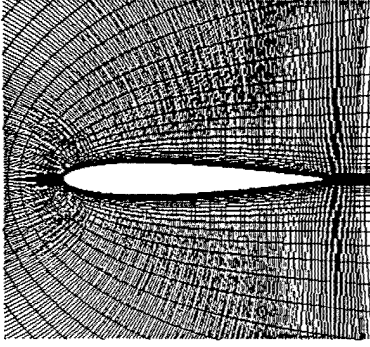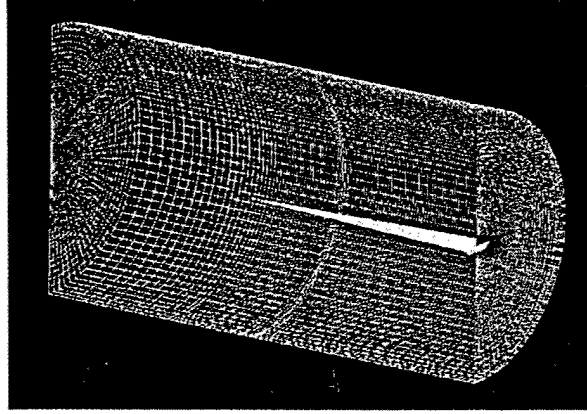
9

Figure1. High-quality grids for 2-D airfoil

Figure 2. High-quality grids for 3-D Delta wing

2.3 High-order compact scheme and high-order filter

The governing equations are discretized in time by implicit method based on second order Euler Backward scheme. The sixth-order centered compact difference scheme is used for spatial derivatives. High-order compact filter is employed to reduce numerical oscillation.

In Eq. (2.1), a second order Euler Backward scheme is used for time derivatives, and the fully implicit form of the discretized equations is given by

$$\frac{3Q^{n+1} - 4Q^n + Q^{n-1}}{2J\Delta t} + \frac{\partial\left(E^{n+1} - E_v^{n+1}\right)}{\partial \xi} + \frac{\partial\left(F^{n+1} - F_v^{n+1}\right)}{\partial \eta} + \frac{\partial\left(G^{n+1} - G_v^{n+1}\right)}{\partial \zeta} = 0. \quad (2.2)$$

Q^{n+1} is estimated iteratively as:

$$Q^{n+1} = Q^p + \delta Q^p$$

where,

$$\delta Q^p = Q^{p+1} - Q^p$$

At step $p = 0, Q^p = Q^n$; as δQ^p is driven to zero, Q^p approaches Q^{n+1}. The flux vectors are linearized as follows:

$$E^{n+1} \approx E^p + A^p \delta Q^p$$

$$F^{n+1} \approx F^p + B^p \delta Q^p$$

$$G^{n+1} \approx G^p + C^p \delta Q^p$$

So that Eq. (2.2) can be written as:

$$\left[\frac{3}{2}I + \Delta t J\left(D_\xi A + D_\eta B + D_\zeta C\right)\right]\delta Q^p = R \quad (2.3)$$

where R is the residual:

$$R = -\left(\frac{3}{2}Q^p - 2Q^n + \frac{1}{2}Q^{n-1}\right) - \Delta t J\left[D_\xi\left(E - E_v\right) + D_\eta\left(F - F_v\right) + D_\zeta\left(G - G_v\right)\right]^p \quad (2.4)$$

D_ξ, D_η, D_ζ represent partial differential operators, and A, B, C are the Jacobian matrices of flux vectors:

$$A = \frac{\partial E}{\partial Q}, \quad B = \frac{\partial F}{\partial Q}, \quad G = \frac{\partial G}{\partial Q}$$

The right hand side of Eq. (2.3) is discretized using sixth-order compact scheme (Lele, 1992) for spatial derivatives, and the left hand side of the equation will be solved by LU-SGS method (Yoon et al, 1992).

The general form for compact finite difference schemes (Lele, 1992) is given by

$$\beta_- f'_{j-2} + \alpha_- f'_{j-1} + f'_j + \alpha_+ f'_{j+1} + \beta_+ f'_{j+2} = \frac{1}{h}(b_- f_{j-2} + a_- f_{j-1} + c\ f_j + a_+ f_{j+1} + b_+ f_{j+2})$$

(2.5)

For sixth-order compact scheme:

$$\beta_- = 0, \ \alpha_- = \frac{1}{3}, \ \alpha_+ = \frac{1}{3}, \ \beta_+ = 0,$$

$$b_- = -\frac{1}{36}, \ a_- = -\frac{1}{9}, \ a_+ = \frac{1}{9}, \ b_+ = \frac{1}{36}$$

Because of the use of the central difference scheme, two-point ``saw-tooth" oscillations will generally be generated, especially in the low viscous region. Those oscillations can induce some spurious non-physical waves. To avoid this phenomenon, we need to use high-order (8th or 10th order) filter for the solution, which is a different concept from filtering the equation in LES but filtering the solution, at each time step. A compact sixth-order filter can be written as follows:

$$\beta \hat{f}_{j-2} + \alpha \hat{f}_{j-1} + \hat{f}_j + \alpha \hat{f}_{j+1} + \beta \hat{f}_{j+2} =$$

$$a\ f_j + \frac{d}{2}(f_{j+3} + f_{j-3}) + \frac{c}{2}(\ f_{j+2} + f_{j-2}) + \frac{b}{2}\ (f_{j+1} + f_{j-1})$$

(2.6)

where $\hat{f}$ is filtered, f is the original, and

$$\alpha = \frac{5}{8}, \quad \beta = \frac{3-2\alpha}{10}, \quad a = \frac{2+3\alpha}{4}, \quad b = \frac{6+7\alpha}{4}, \quad c = \frac{6+\alpha}{20}, \quad d = \frac{2-3\alpha}{40}. \qquad (2.7)$$

2.4 Efficient Navier-Stokes Solver

We use LU-SGS method (Yoon et al, 1992) to solve the Navier-Stokes equations. The equation can be written as

$$[\frac{3}{2}I + \Delta t J(D_\xi A + D_\eta B + D_\zeta C)]\delta Q^p = R \qquad (2.8)$$

The right-hand-side of Eq.(2.8) is discretized using the fourth-order compact scheme for spatial derivatives. The left-hand-side of Eq.(2.8) is discretized using the LU-SGS method. The Jacobian matrices of flux vectors given by Eq.(2.8) are split as:

$$A = A^+ + A^-, \quad B = B^+ + B^-, \quad C = C^+ + C^-$$

11

where

$$A^\pm = \frac{1}{2}[A \pm r_A I]$$

$$B^\pm = \frac{1}{2}[B \pm r_B I]$$

$$C^\pm = \frac{1}{2}[C \pm r_C I]$$

and

$$r_A = \kappa max[|\lambda(A)|] + \tilde{\nu}$$

$$r_B = \kappa max[|\lambda(B)|] + \tilde{\nu}$$

$$r_C = \kappa max[|\lambda(C)|] + \tilde{\nu}$$

$\lambda(A)$, $\lambda(B)$, $\lambda(C)$ are eigenvalues of A, B, C. The effects of viscous terms are taken into account by adding a constant given by

$$\tilde{\nu} = max[\frac{\mu}{(\gamma-1)M_r^2 R_e P_r}, \frac{4}{3}\frac{\mu}{R_e}] \tag{2.9}$$

The first-order upwind finite difference scheme is used for the split flux terms in the left-hand-side of the Eq.(2.8)

$$[\frac{3}{2}I + \Delta t J(r_A + r_B + r_C)I]\delta Q_{i,j,k}^p = R_{i,j,k}^p$$

$$-\Delta t J \quad [\quad A^- \delta Q_{i+1,j,k}^p - A^+ \delta Q_{i-1,j,k}^p$$

$$+ \quad B^- \delta Q_{i,j+1,k}^p - B^+ \delta Q_{i,j-1,k}^p$$

$$+ \quad C^- \delta Q_{i,j,k+1}^p - C^+ \delta Q_{i,j,k-1}^p \quad] \tag{2.10}$$

Eq.(2.10) is divided into the following three steps and solved by iteration.

Step 1:

$$\delta Q_{i,j,k}^0 = [\frac{3}{2}I + \Delta t J(r_A + r_B + r_C)I]^{-1} R_{i,j,k}^p$$

step 2:

$$\delta Q_{i,j,k}^* = \delta Q_{i,j,k}^0 + [\frac{3}{2}I + \Delta t J(r_A + r_B + r_C)I]^{-1}$$

$$\times[\Delta t J(A^+ \delta Q_{i-1,j,k}^* + B^+ \delta Q_{i,j-1,k}^* + C^+ \delta Q_{i,j,k-1}^*)]$$

step 3:

$$\delta Q_{i,j,k}^P = \delta Q_{i,j,k}^* - [\frac{3}{2}I + \Delta t J(r_A + r_B + r_C)]^{-1}$$

$$\times[\Delta t J(A^- \delta Q_{i+1,j,k}^P + B^- \delta Q_{i,j+1,k}^P + C^- \delta Q_{i,j,k+1}^P)]$$

2.5 High-order weighted compact scheme

In order to capture the shock without elimination of small vortex which is particularly important to DNS for shock-boundary layer interaction, we developed a so-called 'high-order weighted compact scheme'. The details will be described in Chapter 3.

2.6 Non reflecting boundary conditions

In DNS/LES for compressible flow, especially for complex geometry, the properly imposed boundary condition is required to prevent the wave from reflecting at the boundary and contaminating the inner region of a computational domain. The specification of the outflow boundary conditions becomes one of the major difficulties. To avoid reflection of outgoing waves, a buffer domain (Street & Macaraeg, 1989) was introduced adding to the original computational domain at the outflow boundary. The governing equations in the buffer domain have been modified by increasing diffusion in certain direction. Alternatively, a sponge layer approach has been used by a number of authors. Both buffer and sponge zones are capable of absorbing the outward moving waves, and have been used in many DNS/LES computations. But these methods have some shortages. First, extra sponge or buffer areas have to be added to the original domain, which will increase the number of grid points and computational cost. Second, the sponge approach can only be applied when the equations of perturbation are considered, which may not be applicable when the so-called "base flow" does not exist or can hardly be defined. An alternative approach to buffer or sponge method is the non-reflecting boundary condition based on the characteristic analysis. The characteristic boundary conditions for Euler system can be found in a number of literatures. The concept of non-reflecting boundary conditions was proposed by Thompson (1987, 1990), where the idea of specifying the boundary conditions according to the inward and outward propagating waves has been introduced. Usually the outgoing waves have their behavior defined entirely by the solution at and within the boundary, and no boundary conditions are needed. Therefore, the number of boundary conditions is equal to the number of incoming waves. In Thompson's paper, boundary conditions of Euler equations are given for different situations without considering the viscosity effect. The characteristic boundary conditions for Euler system cannot be directly used for Navier-Stokes equations. Actually, there is no characteristic relation in Navier-Stokes system. However, in some circumstances, such as free stream, far field, etc. where the viscosity is less important, the characteristic relation can still be used. Poinsot and Lele (1992) have extended Thompson's method to specify the boundary conditions for the Navier-Stokes equations, where the effect of viscous has been taken into account. However, they only give the expression of boundary conditions in the Cartesian coordinates. Based on the previous work by the above authors, we have developed non-reflecting boundary conditions for compressible flow in curvilinear coordinates (Jiang et al, 1999b). The

13

computation shows our work is completely successful for eliminating non-physical wave reflection. Apparently, it is an original work and important to DNS for curvilinear coordinates. Based on the characteristic analysis, the hyperbolic terms in ξ direction can be modified as:

$$\frac{\partial \rho}{\partial t} + d_1 + V\frac{\partial \rho}{\partial \eta} + \rho(\eta_x\frac{\partial u}{\partial \eta} + \eta_y\frac{\partial v}{\partial \eta} + \eta_z\frac{\partial w}{\partial \eta}) + W\frac{\partial \rho}{\partial \zeta} + \rho(\zeta_x\frac{\partial u}{\partial \zeta} + \zeta_y\frac{\partial v}{\partial \zeta} + \zeta_z\frac{\partial w}{\partial \zeta}) + vis_1 = 0$$

$$\frac{\partial u}{\partial t} + d_2 + V\frac{\partial u}{\partial \eta} + \frac{1}{\rho}\eta_x\frac{\partial p}{\partial \eta} + W\frac{\partial u}{\partial \zeta} + \frac{1}{\rho}\zeta_x\frac{\partial p}{\partial \zeta} + vis_2 = 0$$

$$\frac{\partial v}{\partial t} + d_3 + V\frac{\partial v}{\partial \eta} + \frac{1}{\rho}\eta_y\frac{\partial p}{\partial \eta} + W\frac{\partial v}{\partial \zeta} + \frac{1}{\rho}\zeta_y\frac{\partial p}{\partial \zeta} + vis_3 = 0 \qquad (2.11)$$

$$\frac{\partial w}{\partial t} + d_4 + V\frac{\partial w}{\partial \eta} + \frac{1}{\rho}\eta_z\frac{\partial p}{\partial \eta} + W\frac{\partial w}{\partial \zeta} + \frac{1}{\rho}\zeta_z\frac{\partial p}{\partial \zeta} + vis_4 = 0$$

$$\frac{\partial p}{\partial t} + d_5 + V\frac{\partial p}{\partial \eta} + \gamma p(\eta_x\frac{\partial u}{\partial \eta} + \eta_y\frac{\partial v}{\partial \eta} + \eta_z\frac{\partial w}{\partial \eta}) + W\frac{\partial \rho}{\partial \zeta} + \gamma p(\zeta_x\frac{\partial u}{\partial \zeta} + \zeta_y\frac{\partial v}{\partial \zeta} + \zeta_z\frac{\partial w}{\partial \zeta}) + vis_5 = 0$$

where $vis_1 - vis_5$ represent viscous terms in curvilinear coordinates, and

$$\begin{bmatrix} d_1 \\ d_2 \\ d_3 \\ d_4 \\ d_5 \end{bmatrix} = \begin{bmatrix} \frac{1}{c^2}[\frac{1}{2}(L_1 + L_5) + L_2] \\ \frac{\xi_x}{2\beta\rho c}(L_5 - L_1) - \frac{1}{\beta^2}(\xi_y L_3 + \xi_z L_4) \\ \frac{\xi_y}{2\beta\rho c}(L_5 - L_1) + \frac{1}{\beta^2\xi_x}[(\xi_x^2 + \xi_z^2)L_3 - \xi_z\xi_y L_4] \\ \frac{\xi_z}{2\beta\rho c}(L_5 - L_1) - \frac{1}{\beta^2\xi_x}[\xi_y\xi_z L_3 - (\xi_x^2 + \xi_y^2)L_4] \\ \frac{1}{2}(L_1 + L_5) \end{bmatrix} \qquad (2.12)$$

In (2.12) c is the sound wave speed and $\beta = \sqrt{\xi_x^2 + \xi_y^2 + \xi_z^2}$.

L_i represent the amplitude variations of the characteristic wanes corresponding to the characteristic velocities, which are given by

$\lambda_1 = U - C_\xi$

$\lambda_2 = \lambda_3 = \lambda_4 = U$

$\lambda_5 = U + C_\xi$

where $C_\xi = c\beta$ and

14

$$L_1 = (U - C_\xi)[-\frac{\rho c}{\beta}(\xi_x \frac{\partial u}{\partial \xi} + \xi_y \frac{\partial v}{\partial \xi} + \xi_z \frac{\partial w}{\partial \xi}) + \frac{\partial p}{\partial \xi}]$$

$$L_2 = U(c^2 \frac{\partial \rho}{\partial \xi} - \frac{\partial p}{\partial \xi})$$

$$L_3 = U(-\xi_y \frac{\partial u}{\partial \xi} + \xi_x \frac{\partial v}{\partial \xi}) \tag{2.13}$$

$$L_4 = U(-\xi_z \frac{\partial \bar{u}}{\partial \xi} + \xi_x \frac{\partial w}{\partial \xi})$$

$$L_5 = (U + C_\xi)[\frac{\rho c}{\beta}(\xi_x \frac{\partial u}{\partial \xi} + \xi_y \frac{\partial v}{\partial \xi} + \xi_z \frac{\partial w}{\partial \xi}) + \frac{\partial p}{\partial \xi}]$$

These equations will be used for neighbors of boundary points in ξ direction. The equations for η and ζ directions are similar. In this way, the non-physical wave reflection can be effectively eliminated.

2.7 Effective sub-grid models (Structure-function subgrid model)

Since LES only resolved the large length scales but filtered small length scales, to adopt a right sub-grid model to represent these filtered small length scales becomes particularly important.

The filtered structure-function model is developed by Ducros et al.(1996). The subgrid scale shear stress and heat flux can be modeled as

$$\tau_{kl} = \overline{\rho} \nu_t \left[\left(\frac{\partial \tilde{u}_k}{\partial x_l} + \frac{\partial \tilde{u}_l}{\partial x_k} \right) - \frac{2}{3} \frac{\partial \overline{u}_m}{\partial x_m} \delta_{kl} \right] \tag{2.14}$$

$$q_k = \frac{\gamma \overline{\rho} \nu_t}{Pr_t} \frac{\partial \tilde{T}}{\partial x_k}$$

Here Pr_t is the turbulent Prandtl number taken equal to 0.6 as in isotropic turbulence, ν_t is the turbulent kinetic viscosity defined as

$$\nu_t(x,t) = 0.0014 C_k^{-3/2} \Delta[\tilde{F}_2^{(3)}(x,t)]^{1/2} \tag{2.15}$$

where $\tilde{F}_2^{(3)}$ is the filtered structure function. In the case of flat-plate boundary layer flows with meshes flattened in the wall-normal direction, $\tilde{F}_2^{(3)}$ takes the four-neighbor formulation proposed by Normand and Lesieur (1992).

$$\tilde{F}_2^{(3)} = \frac{1}{4} \left[\left\| \tilde{u}_{i+1,j}^{(3)} - \tilde{u}_{i,j}^{(3)} \right\|^2 + \left\| \tilde{u}_{i-1,j}^{(3)} - \tilde{u}_{i,j}^{(3)} \right\|^2 + \left\| \tilde{u}_{i,j+1}^{(3)} - \tilde{u}_{i,j}^{(3)} \right\|^2 + \left\| \tilde{u}_{i,j-1}^{(3)} - \tilde{u}_{i,j}^{(3)} \right\|^2 \right]$$

where
$$\tilde{u}_{i,j}^{(3)} = HP^{(3)}(\tilde{u}_{i,j})$$

$\Delta = (\Delta_x \Delta_y)^{1/2}$ is used to characterize the grid size, where Δ_x and Δ_y denote the grid size in the streamwise direction and spanwise direction, respectively. C_k is the Kolmogorov constant taking the value of 1.4. $HP^{(3)}$ is a discrete Laplacian filter iterated 3 times, which is served as a high-pass filter before computing the structure function. The first iteration of the Laplacian filter $HP^{(1)}$ is defined by

$$\tilde{u}_{i,j}^{(1)} = HP^{(1)}(\tilde{u}_{i,j}) = \tilde{u}_{i+1,j} - 2\tilde{u}_{i,j} + \tilde{u}_{i-1,j} + \tilde{u}_{i,j+1} - 2\tilde{u}_{i,j} + \tilde{u}_{i,j-1} \qquad (2.16)$$

2.8 MPI parallel computation

Message Passing Interface (MPI, e.g., Pacheco, 1994), which is a standard message-passing library for writing message-passing style parallel programs, provides us a better route to write parallel programs. MPI consists of a small group of functions that are used to support communication among processors. A message-passing function is simply a function that explicitly controls data transmitting from one processor to the other. Because MPI has become a standard library, most existing parallel computers support it. Therefore, an MPI programmer has no need to worry about portability. These computers for MPI include not only distributed-memory parallel computers but also shared-memory parallel computers. Even on workstations, MPI can also be used. This greatly reduces the limitation of parallel application in DNS.

In our previous effort, an MPI parallel code was developed based on our serial code. The parallelism of the DNS code is examined. The performance of the parallel program is examined for our compressible DNS code on an SGI Origin 2000 computer and the results show great computing efficiency of parallel machines with MPI (see Figure 3)
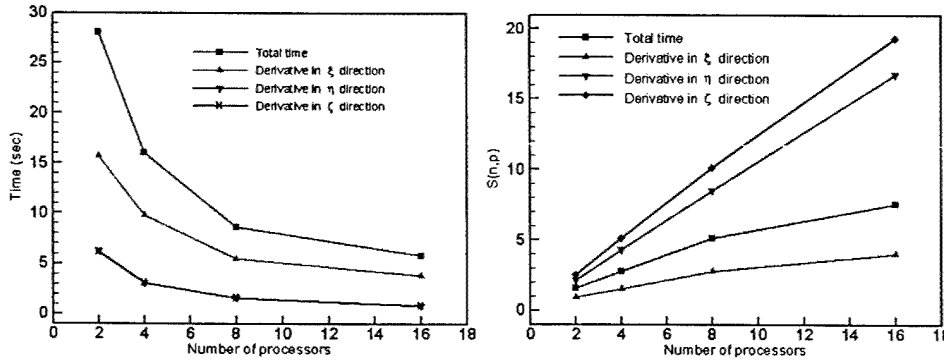
(a) Wall-clock time vs number of processors   (b) Speedup vs number of processors
Figure 3. Linearly Speed up of MPI Computation

In order to maintain good balance data must be uniformly distributed among multiple processors. Here, because the computation is related to each grid point, how to distribute these points among processors, or how to partition the computational domain is very important to improve parallelism. Since MPI code is very portable, our LES code can be used for any parallel machine including our own machine and DOD supercomputers.

Chapter 3

High-Order Weighted Compact Scheme

3.1 High-order Compact Scheme

Recently compact schemes have been widely used in CFD. Standard finite difference schemes need to be at least one point wider than the desired approximation order. It is difficult to find suitable and stable boundary closure for high order schemes. However, the compact scheme can achieve higher order without increasing the stencil width. As the compact scheme has an implicit form and involves neighboring grid point derivative values, additional free parameters can be used not only to improve the accuracy but also to optimize the other properties such as resolution, stability, and conservation. A family of centered compact schemes proposed by LeLe(Lele, 1992) have been proved to have spectral-like resolution. The conservation property is also important, especially for flow with shocks.

Though the advantages of compact schemes are obvious, there are still difficulties in using them to solve problems involving shock waves or discontinuities. When they are used to differentiate a discontinuous function, the computed derivative has grid to grid oscillation. Recently the ENO (Harten, 1987; Shu, 1988, 1989) and WENO (Liu, 1994; Jiang, 1996) schemes have been widely used for shock wave capturing and have been proved very successful. These schemes check the smoothness of the candidate stencils. The ENO scheme selects the smoothest stencil, while the WENO scheme uses all the candidate stencils but with assigned weights. Inspired by the success of the WENO scheme, we have developed a new compact scheme (Jiang et al, 2001a) so that the new compact scheme not only preserves the properties of compact schemes but also can be used for shock wave capturing. This new scheme preserves the characteristic of standard compact schemes achieving high order accuracy and high resolution by a compact stencil. The improvement of this new scheme over the standard compact scheme is that it can accurately capture shock waves without oscillation. The idea of the Weighted Compact Scheme is similar to the WENO scheme (Jiang and Shu 1996). In the WENO scheme, each of the candidate stencils is assigned a weight that determines the contribution of this stencil to the final approximation of the numerical flux. The weights are defined in such a way that in smooth regions it approaches certain optimal weights to achieve a higher order of accuracy, while in regions close to discontinuity, the stencils that contain the discontinuities are assigned a nearly zero weight. Similarly to this idea, the Weighted Compact Scheme is constructed by the combination of the approximations of derivatives on candidate stencils. The stencil that contains the discontinuity has less contribution. In this way, the oscillation near the discontinuity can be reduced, while the characteristics of the compact scheme can still be preserved. The building blocks of the Weighted Compact Scheme are the standard compact schemes. The Weighted Compact Scheme is a hybrid of different forms of standard schemes. Compared to the WENO scheme, this Weighted Compact Scheme can achieve higher order accuracy and higher resolution with the same stencil.

3.2 High-order Weighted compact scheme

For simplicity, we consider a uniformly spaced grid where the nodes are indexed by j. The independent variable at the nodes is $x_j = h(j-1)$ for $1 \le j \le N$ and the function values at the nodes $f_j = f(x_j)$ are given. The finite difference approximation f' to the first derivative of the function f on the nodes can be written in the following general form while the standard compact scheme (Lele, 1992) is used.

$$\beta_- f'_{j-2} + \alpha_- f'_{j-1} + f'_j + \alpha_+ f'_{j+1} + \beta_+ f'_{j+2} = \frac{1}{h}(b_- f_{j-2} + a_- f_{j-1} + cf_j + a_+ f_{j+1} + b_+ f_{j+2})$$

(3.1)

For the point j, we define three candidate stencils containing the point j:

$$S_0 = (x_{j-2}, x_{j-1}, x_j), \quad S_1 = (x_{j-1}, x_j, x_{j+1}), \quad S_2 = (x_j, x_{j+1}, x_{j+2})$$

On each of them we can get a compact scheme. By matching the Taylor series coefficients to various orders, the third and fourth order compact schemes corresponding to each stencil can be derived. The coefficients are given as follows:

$$S_0: \beta_- = \beta, \quad \alpha_- = 2\beta + 2, \quad b_- = -\frac{5}{2}\beta - \frac{1}{2}, \quad a_- = 2\beta - 2, \quad c = \frac{1}{2}\beta + \frac{5}{2},$$

$$S_1: \alpha_- = \frac{1}{4}, \quad \alpha_+ = \frac{1}{4}, \quad a_- = -\frac{3}{4}, \quad a_+ = \frac{3}{4}, \quad c = 0,$$

$$S_2: \beta_+ = \beta, \quad \alpha_+ = 2\beta + 2, \quad b_+ = \frac{5}{2}\beta + \frac{1}{2}, \quad a_+ = -2\beta + 2, \quad c = -\frac{1}{2}\beta - \frac{5}{2},$$

where β is a free parameter. The coefficients that are not listed are set to zero. The schemes corresponding to stencils S_0 and S_2 are third order one-sided schemes, and the scheme corresponding to S_1 is a fourth order centered scheme. With these three sets of coefficients, we get three different equations from Eq. (3.1). These equations are represented by F_0, F_1, F_2. When these equations are assigned specific weights and combined, a new scheme is obtained:

$$F = C_0 F_0 + C_1 F_1 + C_2 F_2$$

where, $C_0 + C_1 + C_2 = 1$. If the weights are properly chosen, the new scheme can achieve a higher order because the additional free parameters are introduced. If we set

$$C_0 = C_2 = \frac{1}{18 - 24\beta}, \quad C_1 = \frac{8 - 12\beta}{9 - 12\beta},$$

(3.2)

the new scheme is at least a sixth order centered compact scheme. This process implies that this sixth order centered compact scheme can be represented by a combination of three lower order schemes. Obviously, the scheme F is a standard compact scheme and

18

cannot avoid the oscillation near the discontinuity. Can we define the weights in such a way that the scheme has the non-oscillatory property? Then the idea of the WENO scheme is introduced to determine the new weight for each stencil. The weights are determined according to the smoothness of the function on each stencil. According to the WENO method, the new weight ω_k is defined as (Jiang and Shu, 1996):

$$\omega_k = \frac{\gamma_k}{\sum_{k=0}^{2} \gamma_k}, \qquad \gamma_k = \frac{C_k}{(\varepsilon + IS_k)^p} \tag{3.3}$$

where, ε is a positive small number that is used to avoid the denominator becoming zero. The smoothness measurement IS_k is defined as following:

$$IS_0 = \frac{13}{12}(f_{j-2} - 2f_{j-1} + f_j)^2 + \frac{1}{4}(f_{j-2} - 4f_{j-1} + 3f_j)^2$$

$$IS_1 = \frac{13}{12}(f_{j-1} - 2f_j + f_{j+1})^2 + \frac{1}{4}(f_{j-1} - f_{j+1})^2 \tag{3.4}$$

$$IS_2 = \frac{13}{12}(f_j - 2f_{j+1} + f_{j+2})^2 + \frac{1}{4}(f_{j+2} - 4f_{j+1} + 3f_j)^2$$

In smooth regions, the following forms can be obtained by a Taylor expansion of (4)

$$IS_0 = \frac{13}{12}(f''h^2) + \frac{1}{4}\left(2f'h - \frac{2}{3}f'''h^3\right)^2 + O(h^6)$$

$$IS_1 = \frac{13}{12}(f''h^2) + \frac{1}{4}\left(2f'h + \frac{1}{3}f'''h^3\right)^2 + O(h^6) \tag{3.5}$$

$$IS_2 = \frac{13}{12}(f''h^2) + \frac{1}{4}\left(2f'h - \frac{2}{3}f'''h^3\right)^2 + O(h^6)$$

If $f' \neq 0$, then

$$IS_0 = (f'h)^2\left[1 + \left(\frac{13f''^2}{12f'} - \frac{f'''}{3}\right)h^2\right] + O(h^6)$$

$$IS_1 = (f'h)^2\left[1 + \left(\frac{13f''^2}{12f'} + \frac{f'''}{6}\right)h^2\right] + O(h^6)$$

$$IS_2 = (f'h)^2\left[1 + \left(\frac{13f''^2}{12f'} - \frac{f'''}{3}\right)h^2\right] + O(h^6)$$

Through a Taylor expansion, it can be easily proved that the new weight ω_k satisfies

$$\omega_0 = C_1\left(1 - \frac{p(fh)^2}{\left(\varepsilon + (fh)^2\right)}\left(\frac{13f''^2}{12f'} - \frac{f'''}{3}\right)h^2\right) + O(h^3)$$

$$\omega_1 = C_2\left(1 - \frac{p(fh)^2}{\left(\varepsilon + (fh)^2\right)}\left(\frac{13f''^2}{12f'} + \frac{f'''}{6}\right)h^2\right) + O(h^3)$$

$$\omega_2 = C_3\left(1 - \frac{p(fh)^2}{\left(\varepsilon + (fh)^2\right)}\left(\frac{13f''^2}{12f'} - \frac{f'''}{3}\right)h^2\right) + O(h^3)$$

Obviously, $\omega_0 - \omega_2 = O(h^3)$; this ensures that the new scheme

$$F = \omega_0 F_0 + \omega_1 F_1 + \omega_2 F_2 \tag{3.6}$$

still can be of sixth order. If $f' = 0$, it can also be proved that the new scheme (3.6) is of sixth order. The conclusion is that the Weighted Compact Scheme (3.6) can preserve the higher order accuracy in the smooth region when the WENO weights are used. According to these definitions, in the smooth region the new scheme is nearly a standard sixth order centered compact scheme. The non-smooth stencil is assigned a small weight so that the non-oscillatory property is achieved. The coefficients of the final Weighted Compact Scheme are given as follows:

$$\beta_- = \beta\omega_0, \quad \alpha_- = (2\beta + 2)\omega_0 + \frac{1}{4}\omega_1, \quad \alpha_+ = (2\beta + 2)\omega_2 + \frac{1}{4}\omega_1, \quad \beta_+ = \beta\omega_2,$$

$$b_- = \left(-\frac{5}{2}\beta - \frac{1}{2}\right)\omega_0, \quad a_- = (2\beta - 2)\omega_0 - \frac{3}{4}\omega_1, \quad c = \left(\frac{1}{2}\beta + \frac{5}{2}\right)\omega_0 - \left(\frac{1}{2}\beta + \frac{5}{2}\right)\omega_2, \tag{3.7}$$

$$a_+ = (-2\beta + 2)\omega_2 + \frac{3}{4}\omega_1, \quad b_+ = \left(\frac{5}{2}\beta + \frac{1}{2}\right)\omega_2$$

If $\beta = 0$, the scheme is tridiagonal; otherwise, it is pentadiagonal. The free parameter β can be used to optimize the scheme when the properties of high resolution, conservation, and stability are concerned. From the above, we can find that the weights play a very important role in the Weighted Compact Scheme. They can be used to optimize the accuracy. In addition, these weights can make the new scheme non-oscillatory. In this proposed project.

3.3 Computational Results for rectangular grids

1) Convection Equation
We first solve the following model equation with different initial functions
$$u_t + u_x = 0 \qquad -1 \le x \le 1$$
$$u(x,0) = u_0(x) \quad \textit{periodic with a period of 2} \tag{3.8}$$
The initial functions are

(1) $u_0(x) = \sin(\pi x),$ (2) $u_0(x) = \sin^4(\pi x),$ (3) $u_0(x) = \begin{cases} 1 & -\dfrac{1}{5} \leq x \leq \dfrac{1}{5}, \\ 0 & otherwise \end{cases}$

(4) $u_0(x) = \begin{cases} \left[1 - \left(\dfrac{10}{3} x \right)^2 \right]^{1/2} & -\dfrac{3}{10} \leq x \leq \dfrac{3}{10}, \\ 0 - & otherwise \end{cases}$ (5) $u_0(x) = e^{-300 x^2}$

N	L_1 error	L_1 order
20	2.03D-4	
40	3.01D-6	6.07
80	4.59D-8	6.04
160	6.17D-10	6.23

Table 1

N	L_1 error	L_1 order
20	1.29D-2	
40	2.11D-4	5.93
80	3.15D-6	6.06
160	4.32D-8	6.19

Table 2

Tables 1 and 2 list the errors and orders of accuracy in the L_1 norm between the numerical result and the exact solution at time $t = 1$ for initial functions (1) and (2), respectively. N is the number of grid points. High order accuracy for these two smooth initial functions has been achieved.

Figures 4-6 illustrate the results at $t = 0.5$ for initial functions (3), (4), and (5). Clearly, there is no numerical oscillation observed in the region near the discontinuity.
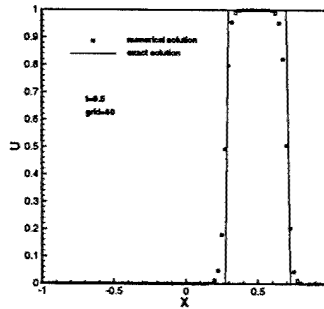
Figure 4. The solution at $t = 0.5$ Figure 5. The solution at $t = 0.5$ Figure 6. The solution at $t = 0.5$
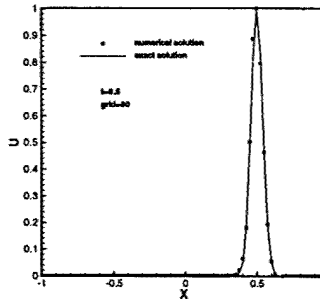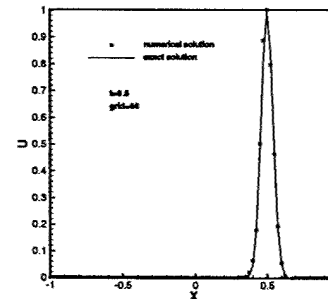
2) Burgers' Equation

The Weighted Compact Scheme is applied to the nonlinear Burgers' equation. With the given initial condition, the exact solution will develop a moving shock wave.

$$u_t + \left(\frac{1}{2}u^2\right)_x = 0 \qquad -1 \le x \le 1$$

$$u(x,0) = \frac{1}{2} + \sin(\pi x) \quad \textit{periodic with a period of 2}$$

Fig.7 (a) and (b) show the wave at different times. The shock appears at $t = 0.55$ and is accurately captured by the scheme. No obvious oscillation is observed.
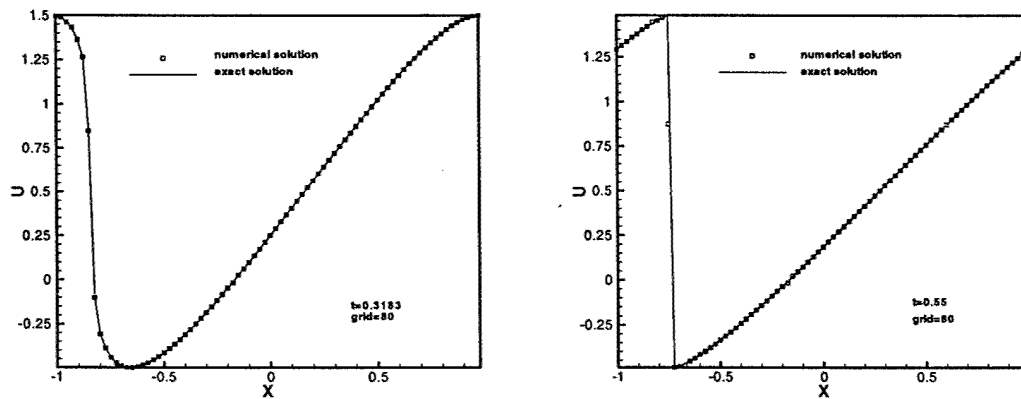
Figure 7. The solution of Burgers' equation at (a) $t = 0.3183$ and (b) $t = 0.55$

3) Euler Equation

We have applied the scheme to the Euler equation. The equations are:

$$\frac{\partial U}{\partial t} + \frac{\partial F}{\partial x} = 0$$

$$U = (\rho, \rho u, E)^T, \quad F = (\rho u, \rho u + p, u(E + p))^T \tag{3.9}$$

The initial conditions are:

$$U_0 = \begin{cases} (1, 0, 1) & x < 0 \\ (0.125, 0, 0.1) & x \ge 0 \end{cases}$$

The results are shown in Fig. 8.

(a)   (b)
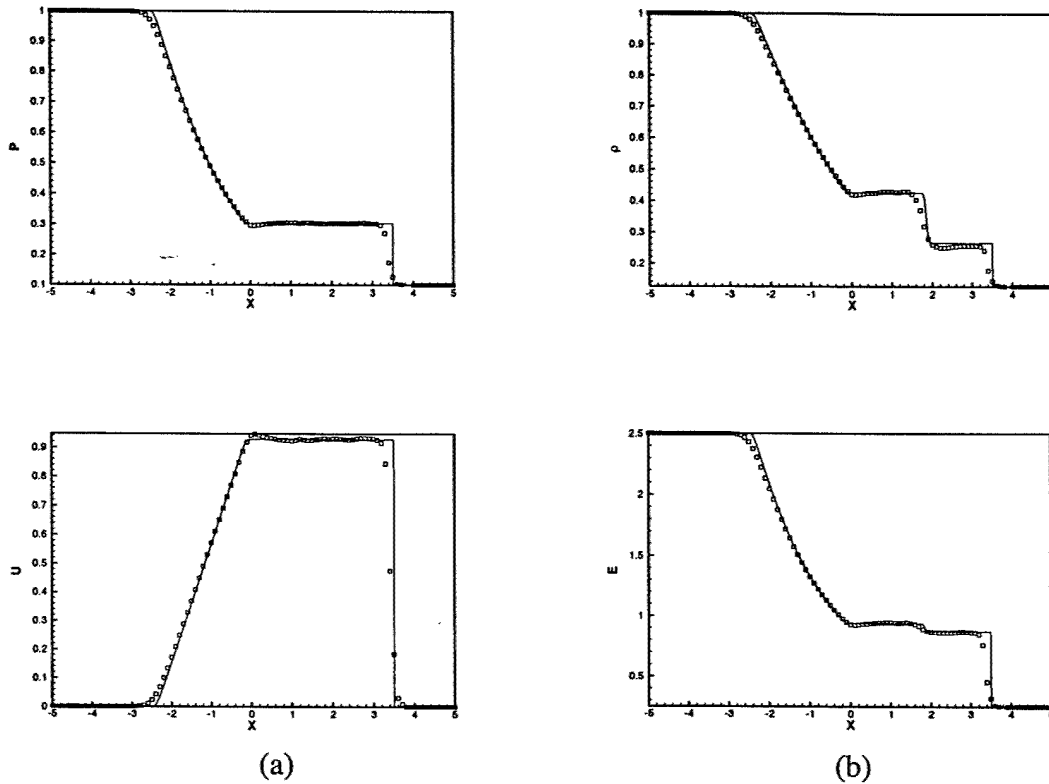
Figure 8. The shock wave solutions of Euler equation at $t = 2$. Number of points = 100. From these preliminary applications of the new Weighted Compact Scheme, we can see the prospects of this new scheme. When the scheme is optimized for optimal resolution and conservation, the shock-capturing property should be much better.

3.4 Computational results for 2-d curvilinear grids

For 2-d curvilinear coordinates, several testing cases have been conducted. The results show that the Weighted Compacted Scheme we developed (Jiang et al, 2001a) can be used for curvilinear coordinate system. The medium distortion of the grid doesn't have much effect on the solutions.

1) Shock-fluctuation interaction problem
2D Euler equations are solved with the following initial conditions:

$$pre-shock: x > 1 \quad u_1 = -c_1 \sin\theta\cos(xk\cos\theta + yk\sin\theta)$$

$$v_1 = -c_1 \cos\theta\cos(xk\cos\theta + yk\sin\theta)$$

$$\rho_1 = 1$$

$$p_1 = 1$$

$$post-shock: x < 1 \quad u_2 = \frac{2(M^2-1)}{(\gamma+1)M^2}u_s$$

$$v_2 = 0$$

$$\rho_2 = \frac{(\gamma+1)M^2}{2+(\gamma-1)M^2}\rho_1$$

$$p_2 = (1 + \frac{2\gamma(M^2-1)}{\gamma+1})p_1$$

where M=8, which indicates a very strong shock wave. The following Figure 9 show the results obtained on different grids. It can be seen that the sharpness of the shock is kept very well even the grid is distorted.
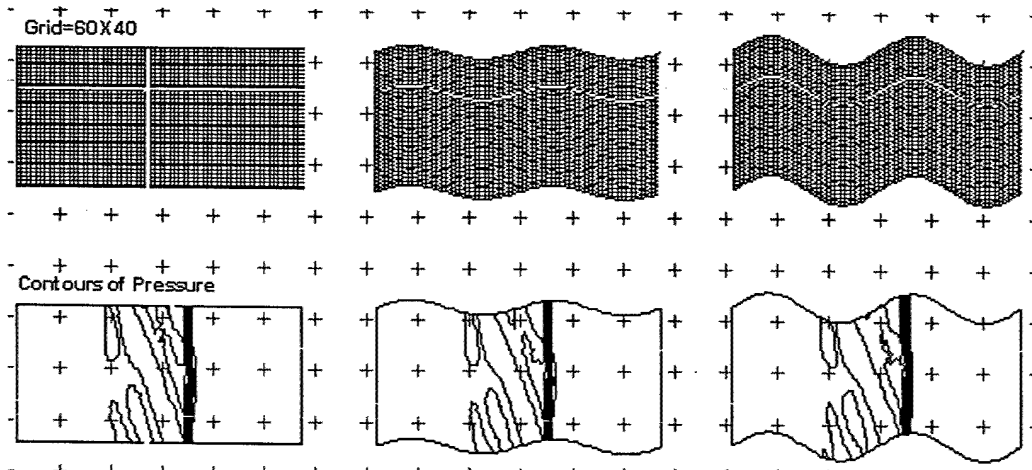
Figure 9. Comparison between rectangular and curvilinear grids for shock fluctuation

2) Vortex pairing in a mixing layer

Vortex pairing process is forced by adding velocity disturbances to the initial mean velocity profile with opposite free-stream.

Mean flow and temperature fields are given by

$$\bar{u} = \tanh(2y)$$

$$\bar{T} = 1 + \frac{\gamma-1}{2}M^2(1-\bar{u}^2)$$

Disturbances are added as

$$u' = -A_1\frac{yL_x}{2\pi B}\cos\left(\frac{4\pi x}{L_x}\right)\exp\left(\frac{-y^2}{B}\right) - A_2\frac{yL_x}{\pi B}\cos\left(\frac{2\pi x}{L_x}\right)\exp\left(\frac{-y^2}{B}\right)$$

$$v' = A_1\sin\left(\frac{4\pi x}{L_x}\right)\exp\left(\frac{-y^2}{B}\right) + A_2\sin\left(\frac{2\pi x}{L_x}\right)\exp\left(\frac{-y^2}{B}\right)$$

24

where $A_1 = 0.05$, $A_2 = 0.025$, $B = 10$, $L_x = 20$, $L_y = 40$, $Re = 2000$, $M = 0.8$.

The following Figure 10 show the appearance of the shock waves and their interactions with the vortices. The results show that the position and the shapes of the shock waves are not affect by the distortion of the grid.
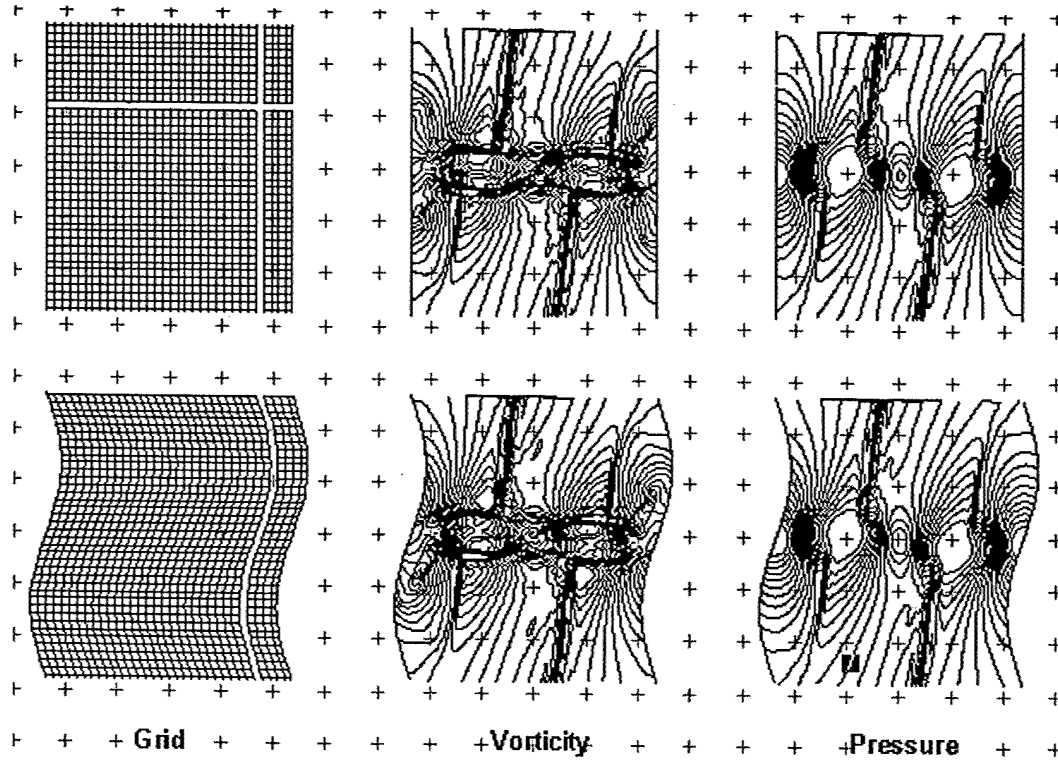
Figure 10. Comparison between rectangular and curvilinear grids for vortex pairing

Conclusion

The weighted compact scheme can preserve the high order accuracy in the smooth area while has no oscillation for discontinuity (shocks). The scheme works well for both rectangular and curvilinear grids.

Chapter 4

DNS for Flow Separation and Transition around Airfoils with Attack Angles

Flow transition in separation bubbles is a classic topic and has been studied for many years (Boiko et al, 2002). However, most of work was focused on flow around a hump placed on a flat plate (Musad et al, 1994) or for a blunt leading edge (Yang & Voke, 2001). Flow separation and transition around an airfoil with attacked angle is rarely found in literature due to its complexity. The linear stability theory (LST; see Drazin & Reid, 1981) is mainly a local analysis with assumption of parallel base flow. The parabolized stability equations (PSE; see Bertolotti, 1992) assume a steady base flow with no elliptic part. These assumptions do not apply for the case of flow separation and transition around airfoil with attack angle where no steady base flow exists and the transition process is dominated by an elliptic process especially in the late stages. Though it is true that the LST and PSE cannot provide a correct prediction for the case, the Kelvin-Helmoholtz instability mechanism in a separated shear layer, which is obtained by inviscid stability theory, still dominates in the early transition stage.

Boundary layer separation and transition exist in many engineering flows around wings and blades. When an adverse pressure on a laminar boundary layer over a surface is strong enough, the laminar boundary layer separates from the surface. Separation and transition in these types of flows are strongly coupled. The instability at the separation zone is widely accepted as dedicated by the Kelvin-Helmholtz mechanism. Transition takes place owing to nonlinear breakdown of spatially growing traveling waves in the separated free shear layer (Yang & Voke, 2001). When the shear layer becomes turbulent, the detached shear layer may reattach to the surface, creating a separation bubble and forming attached turbulent boundary layer. Obviously, the length of the bubble is closely related to when and where the transition takes place. On the other hand, the size of the bubble could directly affect the flight characteristics of the airfoil and the efficiency of the turbine machine. The flow separation over a wing in flight will cause loss of the lift and increase of the drag which threatens the stability and efficiency of the aircraft. Understanding the mechanism of the separation and transition is of great importance in improving design in aircraft and turbo-machinery.

With the development of computer resources and efficient numerical methods, high resolution and high accuracy direct numerical simulation has been becoming feasible on flow separation and transition around airfoil with low Reynolds number. In this work, high-accuracy and high-resolution numerical simulations are conducted to investigate the details of separation and transition processes on a NACA 0012 airfoil The organization of the paper is described as follows. In section 1 and 2, the governing equations and numerical methods will be introduced briefly. In section 3, the definition of the study case and the computational set up will be given. In section 4, the computational results will be presented and analyzed.

4.1 Governing Equations

The three-dimensional compressible Navier-Stokes equations in generalized curvilinear coordinates (ξ, η, ζ) are written in conservative forms:

$$\frac{1}{J}\frac{\partial Q}{\partial t} + \frac{\partial(E - E_v)}{\partial \xi} + \frac{\partial(F - F_v)}{\partial \eta} + \frac{\partial(F - F_v)}{\partial \zeta} = 0 \qquad (4.1)$$

The vector of conserved quantities Q, inviscid flux vector (E, F, G), and viscous flux vector (E_v, F_v, G_v) are defined via

$$Q = \begin{pmatrix} \rho \\ \rho u \\ \rho v \\ \rho w \\ E_t \end{pmatrix}, \quad E = \frac{1}{J}\begin{pmatrix} \rho U \\ \rho U u + p\xi_x \\ \rho U v + p\xi_y \\ \rho U w + p\xi_z \\ U(E_t + p) \end{pmatrix}, \quad F = \frac{1}{J}\begin{pmatrix} \rho V \\ \rho V u + p\eta_x \\ \rho V v + p\eta_y \\ \rho V w + p\eta_z \\ V(E_t + p) \end{pmatrix}, \quad G = \frac{1}{J}\begin{pmatrix} \rho W \\ \rho W u + p\zeta_x \\ \rho W v + p\zeta_y \\ \rho W w + p\zeta_z \\ W(E_t + p) \end{pmatrix},$$

$$E_v = \frac{1}{J}\begin{pmatrix} 0 \\ \tau_{xx}\xi_x + \tau_{yx}\xi_y + \tau_{zx}\xi_z \\ \tau_{xy}\xi_x + \tau_{yy}\xi_y + \tau_{zy}\xi_z \\ \tau_{xz}\xi_x + \tau_{yz}\xi_y + \tau_{zz}\xi_z \\ Q_x\xi_x + Q_y\xi_y + Q_z\xi_z \end{pmatrix}, \qquad F_v = \frac{1}{J}\begin{pmatrix} 0 \\ \tau_{xx}\eta_x + \tau_{yx}\eta_y + \tau_{zx}\eta_z \\ \tau_{xy}\eta_x + \tau_{yy}\eta_y + \tau_{zy}\eta_z \\ \tau_{xz}\eta_x + \tau_{yz}\eta_y + \tau_{zz}\eta_z \\ Q_x\eta_x + Q_y\eta_y + Q_z\eta_z \end{pmatrix},$$

$$G_v = \frac{1}{J}\begin{pmatrix} 0 \\ \tau_{xx}\zeta_x + \tau_{yx}\zeta_y + \tau_{zx}\zeta_z \\ \tau_{xy}\zeta_x + \tau_{yy}\zeta_y + \tau_{zy}\zeta_z \\ \tau_{xz}\zeta_x + \tau_{yz}\zeta_y + \tau_{zz}\zeta_z \\ Q_x\zeta_x + Q_y\zeta_y + Q_z\zeta_z \end{pmatrix}$$

where $J = \dfrac{\partial(\xi, \eta, \zeta)}{\partial(x, y, z)}$ is Jacobian of the coordinate transformation between the curvilinear (ξ, η, ζ) and Cartesian (x, y, z) frames, and $\xi_x, \xi_y, \xi_z, \eta_x, \eta_y, \eta_z, \zeta_x, \zeta_y, \zeta_z$ are coordinate transformation metrics. The contravariant velocity components U, V, W are defined as

$$U \equiv u\xi_x + v\xi_y + w\xi_z, \quad V \equiv u\eta_x + v\eta_y + w\eta_z, \quad W \equiv u\zeta_x + v\zeta_y + w\zeta_z.$$

Q_x, Q_y, Q_z in energy equation are defined as

$$Q_x = -q_x + u\tau_{xx} + v\tau_{xy} + w\tau_{xz}$$
$$Q_y = -q_y + u\tau_{xy} + v\tau_{yy} + w\tau_{yz}$$
$$Q_z = -q_z + u\tau_{xz} + v\tau_{yz} + w\tau_{zz}$$

E_t is the total energy. The components of the viscous stress tensor and heat flux are denoted by $\tau_{xx}, \tau_{yy}, \tau_{zz}, \tau_{xy}, \tau_{xz}, \tau_{yz}$, and q_x, q_y, q_z, respectively.

In the dimensionless form, the reference values for length, density, velocities, temperature, pressure and time are $L, \rho_r, U_r, T_r,\ \rho_r U_r^2$, and L/U_r respectively. In this study, the free stream parameters are chosen as reference values. The chord length of the airfoil is used as the reference length. The dimensionless parameters arise from non-dimensional Mach number M_r, Reynolds number R_e, Prandtl number P_r, and the ratio of specific heats γ, are defined respectively as follows

$$M_\infty = \frac{U_r}{\sqrt{\gamma RT}},\ \mathrm{Re} = \frac{\rho_r U_r L}{\mu_r},\ \mathrm{Pr} = \frac{C_p \mu_r}{k_r},\ \gamma = \frac{C_p}{C_v},$$

where R is the ideal gas constant, C_p and C_v are specific heats at constant pressure and constant volume, respectively. Through out this work, $\mathrm{Pr} = 0.7$ and $\gamma = 1.4$. Viscosity is determined according to the Sutherland's law in dimensionless form

$$\mu = \frac{T^{3/2}(1+S)}{T+S},\ S = \frac{110.3K}{T_\infty}$$

The governing system is closed by the equation of state.

$$\gamma M_r^2 p = \rho T$$

$$E_t = \frac{p}{\gamma - 1} + \frac{1}{2}\rho(u^2 + v^2 + w^2)$$

The components of the viscous stress tensor and heat flux in non-dimensional form are as follows:

$$\tau_{ij} = \frac{\mu}{\mathrm{Re}}\left[\left(\frac{\partial u_i}{\partial x_j} + \frac{\partial u_j}{\partial x_i}\right) - \frac{2}{3}\delta_{ij}\frac{\partial u_k}{\partial x_k}\right]$$

$$q_i = -\frac{\mu}{(\gamma-1)M_r^2 \mathrm{Re} P_r}\frac{\partial T}{\partial x_i}$$

4.2 Numerical Methods

The numerical method used in this study has high order accuracy and high resolution. The governing equations are solved using LU-SGS implicit method based on second order Euler Backward scheme. The sixth-order centered compact difference scheme is used for spatial derivatives. The eighth-order compact filter is employed to reduce numerical oscillation.

In Eq. (1), a second order Euler Backward scheme is used for time derivatives, and the fully implicit form of the discretized equations is given by

$$\frac{3Q^{n+1} - 4Q^n + Q^{n-1}}{2J\Delta t} + \frac{\partial(E^{n+1} - E_v^{n+1})}{\partial \xi} + \frac{\partial(F^{n+1} - F_v^{n+1})}{\partial \eta} + \frac{\partial(G^{n+1} - G_v^{n+1})}{\partial \zeta} = 0. \quad (4.2)$$

Q^{n+1} is estimated iteratively as:

$$Q^{n+1} = Q^p + \delta Q^p$$

where,

$$\delta Q^p = Q^{p+1} - Q^p$$

At step $p = 0, Q^p = Q^n$; as δQ^p is driven to zero, Q^p approaches Q^{n+1}. The flux vectors are linearized as follows:

$$E^{n+1} \approx E^p + A^p \delta Q^p$$
$$F^{n+1} \approx F^p + B^p \delta Q^p$$
$$G^{n+1} \approx G^p + C^p \delta Q^p$$

So that Eq. (4.2) can be written as:

$$\left[\frac{3}{2} I + \Delta t J \left(D_\xi A + D_\eta B + D_\zeta C\right)\right] \delta Q^p = R \qquad (4.3)$$

where R is the residual:

$$R = -\left(\frac{3}{2} Q^p - 2 Q^n + \frac{1}{2} Q^{n-1}\right) - \Delta t J \left[D_\xi \left(E - E_v\right) + D_\eta \left(F - F_v\right) + D_\zeta \left(G - G_v\right)\right]^p \quad (4.4)$$

D_ξ, D_η, D_ζ represent partial differential operators, and A, B, C are the Jacobian matrices of flux vectors:

$$A = \frac{\partial E}{\partial Q}, \quad B = \frac{\partial F}{\partial Q}, \quad G = \frac{\partial G}{\partial Q}$$

The right hand side of Eq. (4.3) is discretized using sixth-order compact scheme (Lele, 1992) for spatial derivatives, and the left hand side of the equation is discretized following LU-SGS method (Yoon, et al ., 1992) In this method, the Jacobian matrices of flux vectors are split as:

$$A = A^+ + A^-, \quad B = B^+ + B^-, \quad C = C^+ + C^-$$

where

$$A^\pm = \frac{1}{2}[A \pm r_A I], \quad B^\pm = \frac{1}{2}[B \pm r_B I], \quad C^\pm = \frac{1}{2}[C \pm r_C I]$$

and,

$$r_A = \kappa \max[|\lambda(A)|] + \tilde{v}, \quad r_B = \kappa \max[|\lambda(B)|] + \tilde{v}, \quad r_C = \kappa \max[|\lambda(C)|] + \tilde{v}$$

where $\lambda(A)$, $\lambda(B)$, $\lambda(C)$ are eigenvalues of A, B, C respectively, κ is a constant greater than 1. $\tilde{v}$ is taken into account for the effects of viscous terms, and the following expression is used:

$$\tilde{v} = \max\left[\frac{\mu}{(\gamma - 1)M_r^2 R_e P_r}, \frac{4}{3}\frac{\mu}{R_e}\right]$$

The first-order upwind finite difference scheme is used for the split flux terms on the left hand side of Eq. (4.3). This does not affect the accuracy of the scheme when solutions are converged. As the left hand side is driven to zero, the discretization error will also be driven to zero. The finite difference representation of Eq. (4.3) can be written as:

$$\left[\frac{3}{2} I + \Delta t J \left(r_A + r_B + r_C\right) I\right] \delta Q_{i,j,k}^p$$

$$+ \Delta t J \left[A^- \delta Q_{i+1,j,k}^p - A^+ \delta Q_{i-1,j,k}^p + A^- \delta Q_{i+1,j,k}^p - A^+ \delta Q_{i-1,j,k}^p + A^- \delta Q_{i+1,j,k}^p - A^+ \delta Q_{i-1,j,k}^p\right]$$

$$= R_{i,j,k}^p \qquad (4.5)$$

In LU-SGS method, Eq. (4.5) is solved with three steps. First initialize δQ^0 using

$$\delta Q_{i,j,k}^0 = \left[\frac{3}{2} I + \Delta t J (r_A + r_B + r_C) I \right]^{-1} R_{i,j,k}^n$$

In the second step, the following relation is used:

$$\delta Q_{i,j,k}^* = \delta Q_{i,j,k}^0 + \left[\frac{3}{2} I + \Delta t J (r_A + r_B + r_C) I \right]^{-1} \Delta t J \left[A^+ \delta Q_{i-1,j,k}^* + B^+ \delta Q_{i,j-1,k}^* + C^- \delta Q_{i,j,k-1}^* \right]$$

For the last step, δQ^p is obtained by

$$\delta Q_{i,j,k}^p = \delta Q_{i,j,k}^* - \left[\frac{3}{2} I + \Delta t J (r_A + r_B + r_C) I \right]^{-1} \Delta t J \left[A^- \delta Q_{i+1,j,k}^p + B^- \delta Q_{i,j+1,k}^p + C^- \delta Q_{i,j,k+1}^p \right]$$

The sweeping of the computational domain is performed along the planes of $i + j + k = const$, i.e. in the second step, sweeping is from the low-left corner of the grid to the upper-right corner, and then vice versa in the third.

Parallel computation based on Message Passing Interface has been utilized to improve the performance of the code. The parallel computation is combined with the domain decomposition method. The computational domain is divided into n equal-sized sub-domains along ξ direction which is usually the streamwise direction. The details of the numerical methods and parallel computation can be referred to our previous work (Jiang, et al, 1999a; Shan, et al, 2001).

4.3 Problem Definitions and Boundary Conditions

Numerical simulations are performed on a NACA0012 airfoil at attack angle of 4^0. Free stream velocity U_∞, pressure p_∞, temperature T_∞ and chord length of the airfoil C are selected as reference velocity, pressure, temperature and length respectively, which are used to non-dimensional governing equations. The computational domain is plotted in Figure 11. The upstream boundary is 3 chord lengths away from the leading edge of the airfoil. The upper and lower boundaries are about 4 chord length from the solid surface. The outflow boundary is 2 chord lengths downstream of the trailing edge. The airfoil is regarded as infinitely long in the spanwise direction. In our simulations, spanwise length is set as $L_y = 0.1C$ and periodic boundary condition is imposed at the spanwise boundaries.
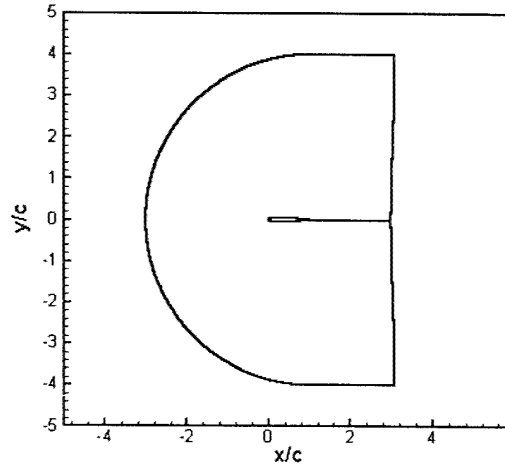
Figure 11. Computational domain

The flow and computational conditions are listed in Table 3. The Reynolds Number based on free stream velocity and chord length is $R_e = 10^5$. Free stream Mach Number is $M_\infty = 0.2$. The numbers of grid point in ξ, η, ζ directions are $N_x = 1200$, $N_y = 32$, $N_z = 180$ respectively. Grid distributions in the (x, z) plane and on the airfoil surface are shown in Figure 12. Grids are uniform in the spanwise direction and stretched in the wall-normal direction. C-grid is used in the (x, z) plane. The grid sizes in wall unit are also listed in Table 3. Parallel computing is based on domain decomposition. The computational domain is divided evenly into N sub-domains along ξ direction when N processors are used. In this work, 24 processors are used.

$Re=U_\infty C/\upsilon_\infty$	M_∞	AOA	$N_x \times N_y \times N_z$	Δx^+	Δy^+	Δz^+
10^5	0.2	4^0	$1200 \times 32 \times 180$	< 13	<15	< 1

Table 3. Flow and computational conditions
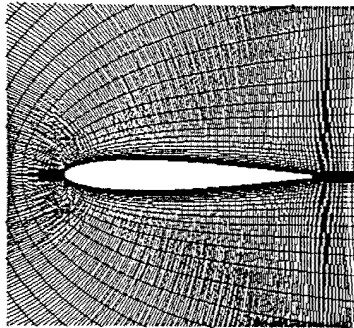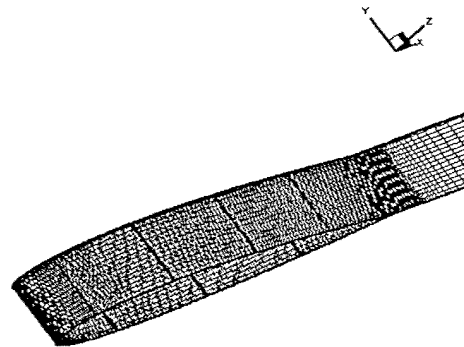
(a) Grid in (x, z) plane   (b) Grid on the airfoil surface
Figure 12. Grid distribution (one out of three grid point is shown)

31

As the flow is subsonic in free stream, the uniform free stream velocities and temperature are prescribed at upstream and far field boundaries. Then density is decided by non-reflecting boundary condition developed in our previous work (Jiang, et al, 1999a). Non-slip, adiabatic boundary condition is used on the surface of the airfoil. Non-reflecting boundary condition is applied to the outflow boundary.

4.4 Results and Analysis

In this study, simulation is carried out with a time step equal to $8.35 \times 10^{-5} C/U_\infty$. The corresponding CFL number is around 400. 2D solutions are used as the initial field. The time integration has reached $t = 3.474 C/U_\infty$. Mean values are obtained by performing averaging in the spanwise direction and in time over a period of $3C/U_\infty$.

4.4.1 2D instability waves and vortex shedding

2D instability waves and vortex shedding appear in both 2D and 3D simulations. The generation and growing of 2D instability waves is the initial stage of the transition. In 2D simulation, because of the lack of 3D motions, we can not see the late stage of transition and breakdown. But the 2D simulation can provide us important information on how the instability waves develop and grow. 2D simulation starts from a uniform flow field. This initial field is not the solution of the governing equations and may bring in some disturbances (initial disturbance brought by numerical initial condition). When perturbations introduced by the initial field can not dissipate through the time integration, they may trigger the most unstable instability waves. This is the reason why we see unsteady behaviors in the simulation although all boundary conditions are steady and no external disturbances are enforced. Flow separation and vortex shedding appear on the suction surface of the airfoil (Figure 13), where a separated mixing layer and vortex shedding are clearly demonstrated by plotting contours of instantaneous spanwise vorticity. The separation zone can be seen clearly from the time averaged velocity vectors shown in Figure 14, but no re-attachment is observed for 2-D simulation (2-D simulation cannot represent the real physics). The 2D solutions are well developed and quasi-periodic behavior is built up. It can be seen clearly that the boundary layer separates from the airfoil surface and develops to unstable shear layer which leads to vortex shedding. These large vortex structures travel downstream along the airfoil surface. There is no vortex breakdown observed in 2D simulation since breakdown is a 3-D and non-linear interaction. This shows 2D direct simulation can only predict the early instability stage, but cannot reveal the 3D mechanism of flow transition.
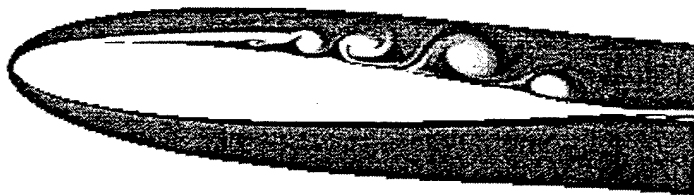
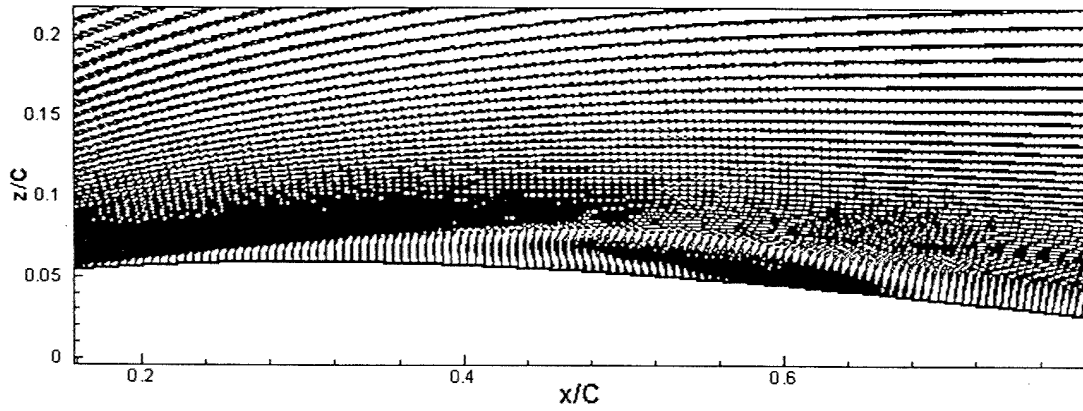Figure 13 Contours of spanwise vorticity from 2D solution

Figure 14 Time averaged velocity field

Note that we did not add any disturbance at inflow, there is a question raised what kind of disturbance triggers the instability wave inside the separated free shear layer? Figure 15 shows time history of fluctuation pressure at different locations. We can see that the pressure fluctuating appears first at $x/c = 1.048$ which is located in the wake very close to the trailing edge (we call it 'wake instability'). As we mentioned above that the disturbances introduced by initial field may excite the most unstable instability wave. However, from the simulation results, we find that large pressure oscillations appear first in the wake very close to the trailing edge. It is because wake is generated by a free shear layer with inflection points but without solid wall even nearby unlike the boundary layer or separated mixing layer, which makes the wake most unstable. The time dependent behaviors of streamwise velocity at different streamwise locations are given in Figure 16, which also confirms that the wake becomes unstable first.
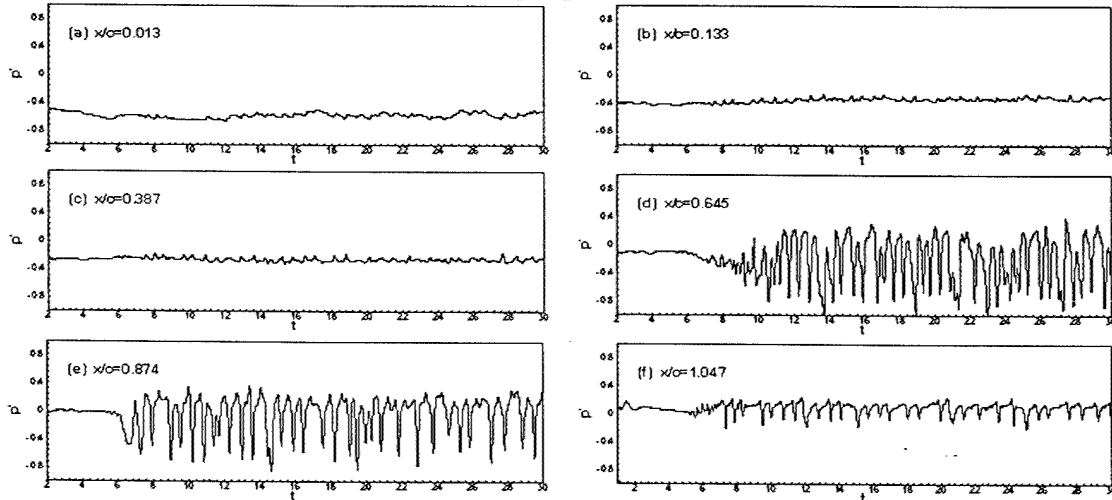
Figure 15. Time history of pressure fluctuation at different locations

33
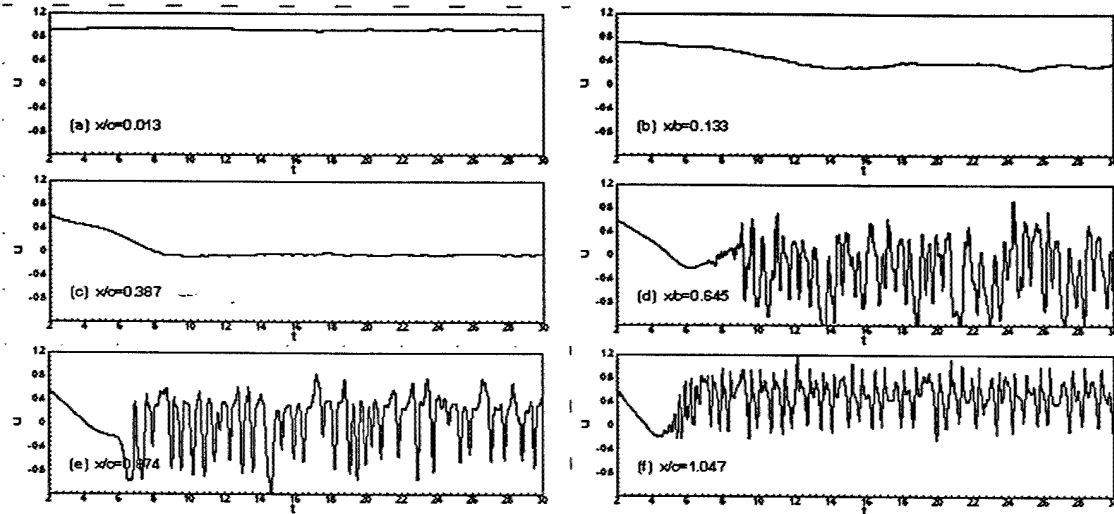
Figure 16. Time history of streamwise velocity at different locations

Then disturbances generated in wake near the trailing edge propagate upstream through acoustic waves. These upward traveling disturbances could change the pressure distribution on the surface. Then, the separation point and the stagnation point become unstable (we call it 'stagnation instability'). The disturbances generated at these locations convected downstream inside the separated shear layer as vortical disturbances. The shear layer has inflected profile with strong reverse flow which subjects to inviscid shear layer instability with much larger growth rate than the viscous counterpart. Figure 17 shows the profiles for the mean streamwise velocity at different locations. Some DNS results shows that the shear layer has absolute instability when backflows are as high as 15-20% of external velocity (Yang & Voke, 2001). From Figure 17 we can see that the reverse velocity reaches 8% of freestream velocity at $x/C = 0.4$, which is a way below the absolute instability range, but at this point we still can see obvious unsteadiness. The disturbances are rapidly amplified in the shear layer and develop to shed vortex structures. Many authors have related this instability mechanism to the Kelvin-Helmoholtz instability. The condition for the Kelvin-Helmoholtz instability to occur is $0 < Kh < 1.2785$ (Yang & Voke, 2001) where K is the wave number and h is the shear layer thickness. In the present simulation, unsteadiness becomes obvious at about $x/C = 0.4$, where the shear layer thickness is about $h \approx 0.0202C$ and the wavelength is $\lambda \approx 0.115C$. Then we get $Kh = \dfrac{2\pi}{\lambda} h \approx 1.104$, which satisfies the criteria for the Kelvin-Helmoholtz instability to develop.
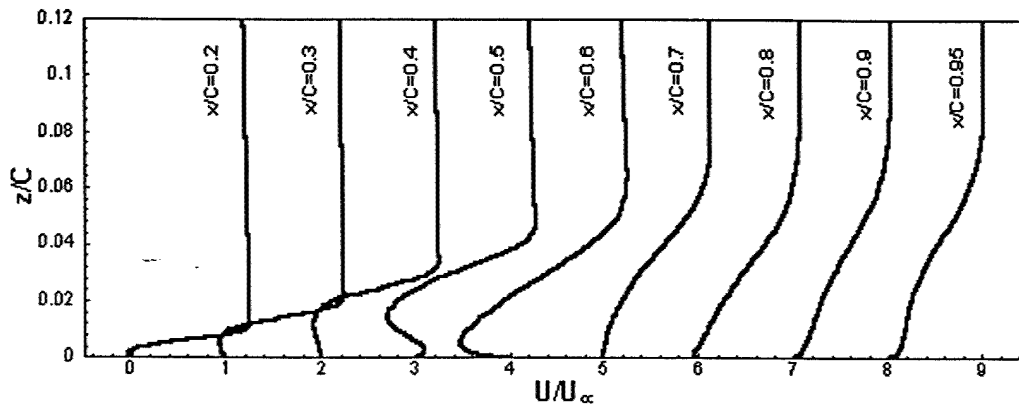
Figure17. Mean velocity profiles at different locations

Figure 18 shows the spectrum of pressure waves at the location close to the wall. The spectrum at different streamwise locations from the leading edge to the trailing edge shows the strong peak at the frequency around $F^+ = 1.4$, which is about the vortex shedding frequency (vortex shedding frequency is changing from time to time). There is a peak at $F^+ \approx 0.3$ which may correspond to so-called low-frequency flapping. As flow is subsonic, acoustic waves travel in both upstream and downstream directions. The pressure field is dominated by the vortex shedding frequency, which is also the frequency of Kelvin-Helmoholtz instability wave. This may provide a clue for flow control that the blowing jet for separation control should have same or similar frequency with very little mass flow (sharp shape in both time and space). When disturbances grow large, nonlinear interactions take place. We can see more high frequencies appear in the spectrum.
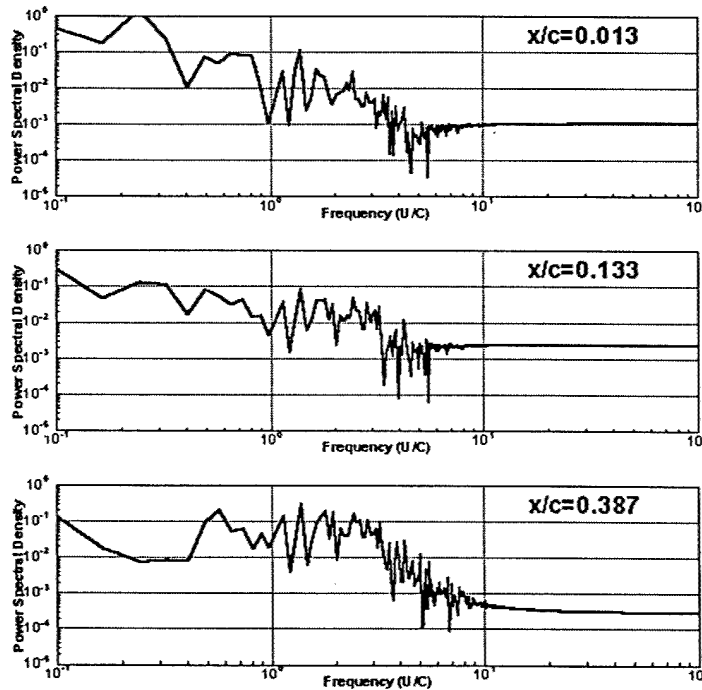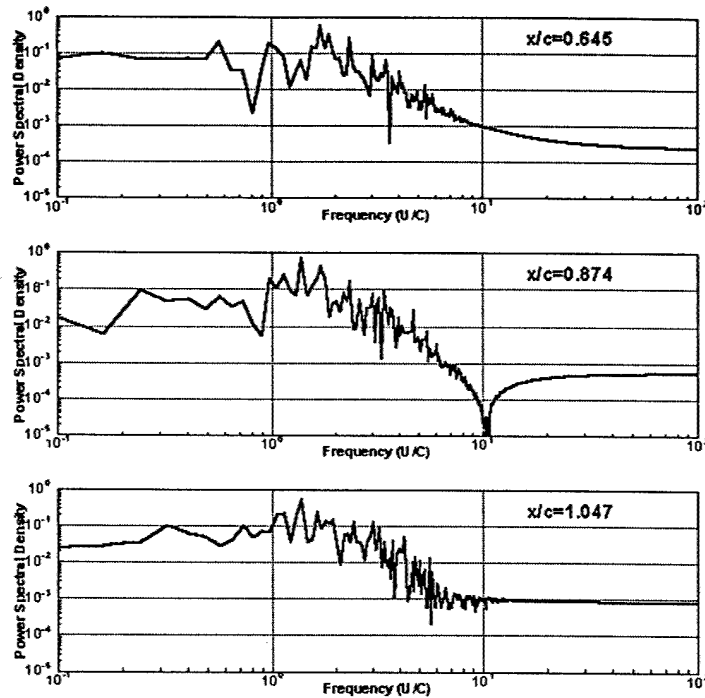
Figure18. Power spectral density of pressure at the mid-boundary layer

4.4.2 Mean flow

3D solutions are highly unsteady. Mean flow characteristics are analyzed first. Figure 19 shows the maximum reverse flow in the wall normal direction along the suction surface. The separated zone appears form $x/C = 0.19$ to $x/C = 0.68$, where the separated laminar boundary evolves into reattached turbulent boundary layer. The reverse flow reaches 8% of free stream velocity at about $x/C = 0.5$. After that the reverse flow appears to be much stronger. From velocity vectors, which are plotted in Figure 20, the separation zone can be identified clearly, which is mush shorter that the 2D sumulation. Reverse flow is very strong near the end of the separation zone.
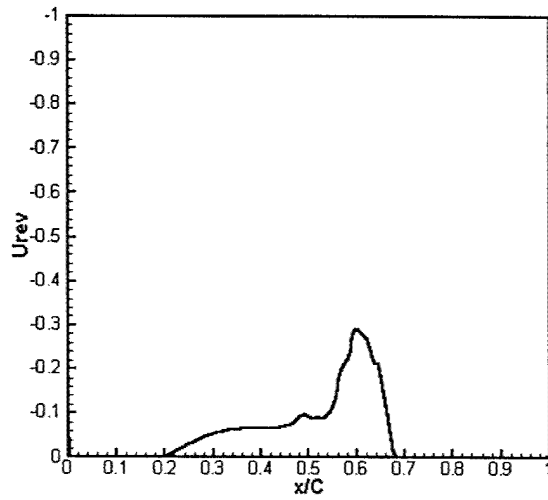
Figure 19. Mean reverse flow distribution on the suction side, $U_{rev} = \min(\overline{u})$
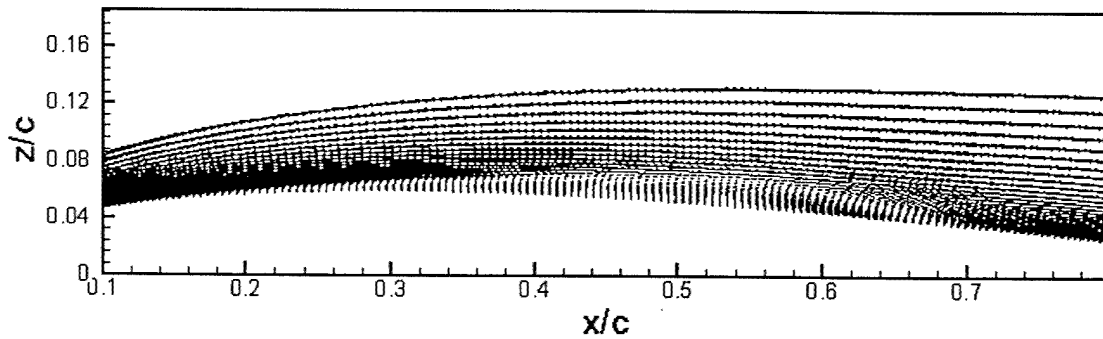
Figure 20. Mean velocity vector

Figure 21 shows the mean pressure coefficient. The flattened region indicates the separation of the boundary layer. The strong adverse pressure gradient at the fore part of the suction surface causes the boundary layer to separate from the surface. In the separation zone, adverse pressure gradient is reduced dramatically. Near the end of the separation zone, large adverse pressure gradient forms again and leads to a rapid increase of reverse flow which is clearly demonstrated in Figure 19. Figure 22 shows the skin friction coefficient of the suction surface. The skin friction increases when transition happens. The separated shear layer becomes turbulent and reattaches to the airfoil surface, forming a closed bubble. As the flow is very unsteady, the shape and the length of the bubble are changing in a large scale. The time averaged length of bubble is about $l_b/C = 0.48$ which can be estimated from Figure 19. After the reattachment, the skin

37

friction coefficient grows rapidly to a high value within a short distance, then stay close to that level with some oscillations which are caused by large vortex structures.
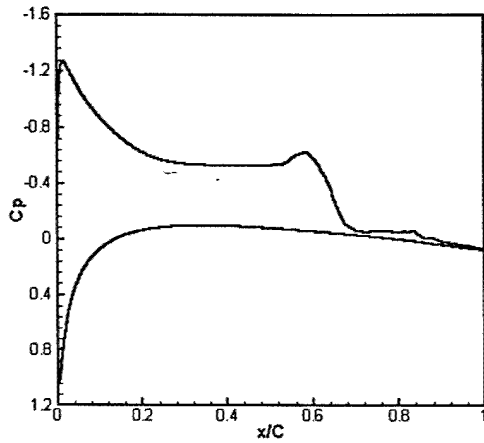
Figure 21. Mean pressure coefficient
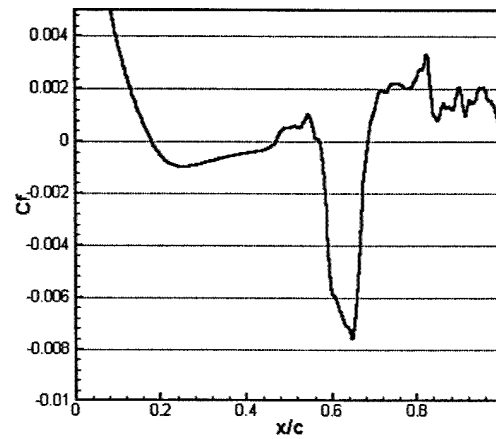
Figure 22. Mean skin friction coefficient

In this simulation, no external disturbance is introduced, yet we observed growth of the disturbance, instability waves and transition. We have discussed in 2D section that according to our observation, the acoustic waves generated near the trailing edge travel upstream, which could change the pressure distribution on the airfoil surface. The stagnation point and the separation point are closely related to pressure distribution and can be unsteady if the pressure distribution changes. The disturbances generated at these points are convected downstream. The separated shear layer is very unstable. The disturbances convected in the shear layer are amplified rapidly. The detached shear layer becomes unstable via the Kelvin-Helmholtz mechanism. Figure 23 shows the maximum the r.m.s. values of fluctuation velocities across the boundary layer along the surface. The growth of disturbances can be seen clearly. Before the separation point $x/C = 0.19$, u' and w' are small but not zero, which indicates that small 2D disturbances exist. The disturbances inside the boundary layer start to growth before the separation point (viscous instability) at around $x/C = 0.2$. Then the disturbance grows in a much faster rate in the separated shear layer corresponding to the inviscid instability at $x/C = 0.2 - 0.4$. u' increases rapidly at about $x/C = 0.4$, where the reverse flow reaches 8% of the free stream velocity. This strong reverse flow makes the shear layer very unstable and leads to the sudden rapid growth of disturbances. Following the sudden growth of u', w', spanwise velocity also starts to grow. The velocity fluctuations reach a maximum value before the mean reattachment point. The rapid growth of velocity fluctuations indicates the appearance of three dimensional motion and nonlinear interaction which leads to breakdown to turbulence. After the breakdown, the separated shear layer reattaches on to the surface and becomes an attached turbulent boundary layer.
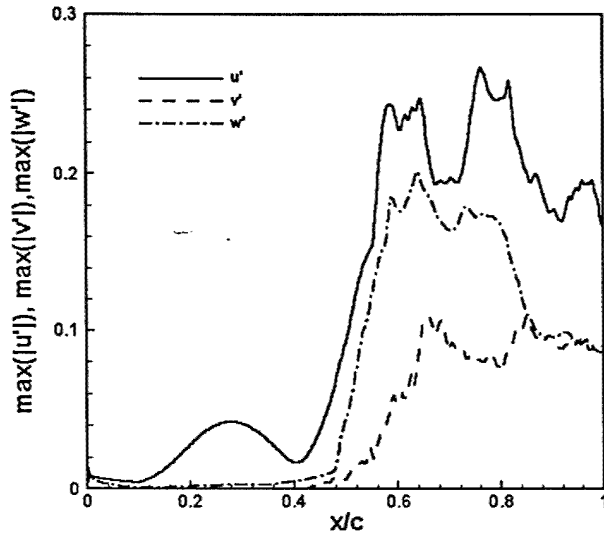
Figure 23. Peak r.m.s across the boundary layer

The mean velocity profiles, the r.m.s fluctuation velocity profiles, and the Reynolds stress are depicted in Figure 24 (a) (b) (c) respectively. In the separation zone, mean velocity profiles demonstrate inflected shapes. After the reattachment, the boundary layer develops to the turbulent velocity profile. The r.m.s fluctuation streamwise velocity profiles at different locations are displayed in (b) which clearly shows the maximum fluctuation happened in the separated shear layer away from the solid surface in normal direction corresponding to the invisid instability much larger than the viscous instability near the solid surface. The first location ($x/C = 0.2$) is very close to the separation point. The peak appears at about the center of the boundary layer. At the following two locations, the fluctuations grow and two peaks show up. From $x/C = 0.5$, the fluctuations grow rapidly and three peaks are found at some locations. This evolution is related to the amplification of the upstream perturbations due to the existence of the inflected velocity profile (invisid instability), vortex shedding and prime vortex breakdown. Profiles of Reynolds stress are shown in (c). Peak values appear inside the boundary layer.
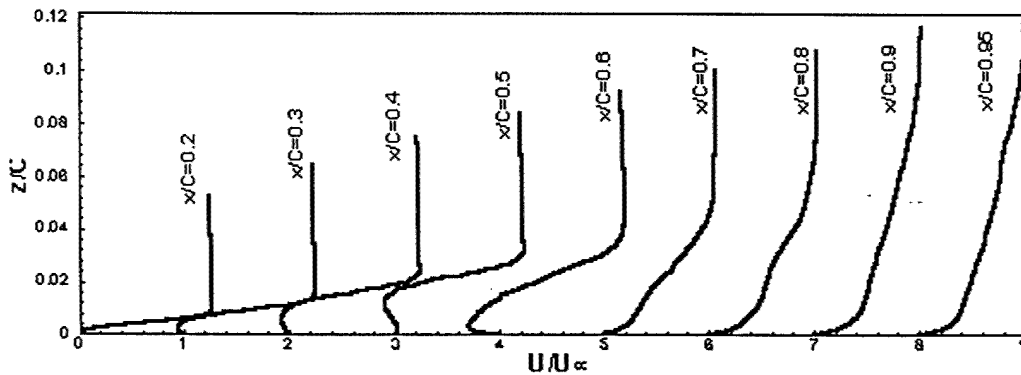
(a) Mean streamwise velocity profiles
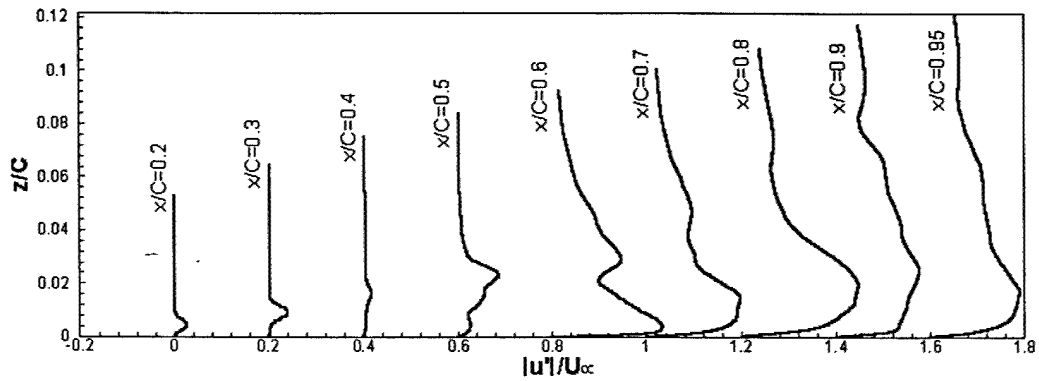
(b) The r.m.s streamwise fluctuation velocity profiles
(Maximum fluctuation happens in the separated shear layer)
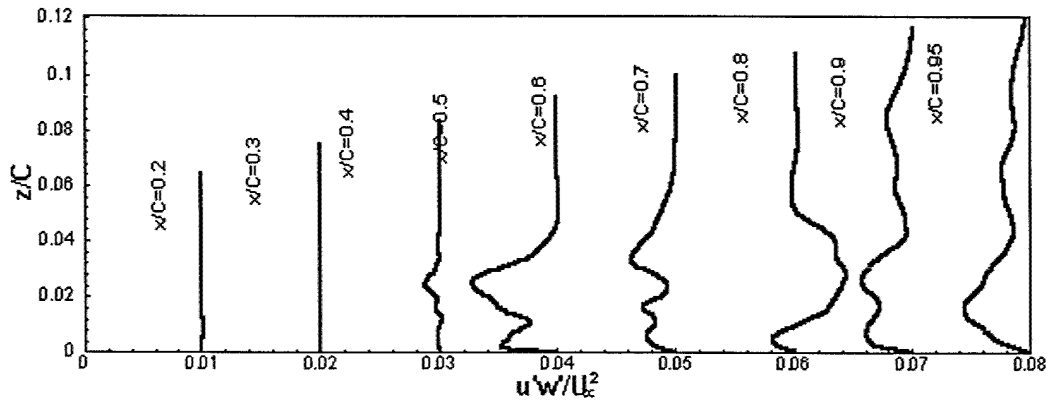
(c) Reynolds stress $\overline{u'w'}$

Figure 24 Statistic profiles

4.4.3 Instantaneous characteristics

Figure 25 shows contours of the instantaneous spanwise vorticity in the middle (x, z) plane. As 3D simulation is started from 2D solutions, the vortex evolution and breakdown can be clearly seen from these time sequent pictures. Before 3D flow is fully built up, instability waves growing in the shear layer and corresponding to vortex shedding can be clearly identified. When run time for 3D simulation is long enough, real 3D motion is fully developed. Nonlinear interactions of velocity fluctuations become very strong and lead to rapid fluctuation growth. Compared with 2D solution in Figure 13, organized vortex shedding disappears and vortex breakdown in very short distance in 3D simulations. It is also shown that 2-D simulation cannot catch the physics for either the flow separation and transition or flow control. The 2-D mechanism is different from the 3-D mechanism and 3-D simulation has to be conducted for flow separation, transition, and control.
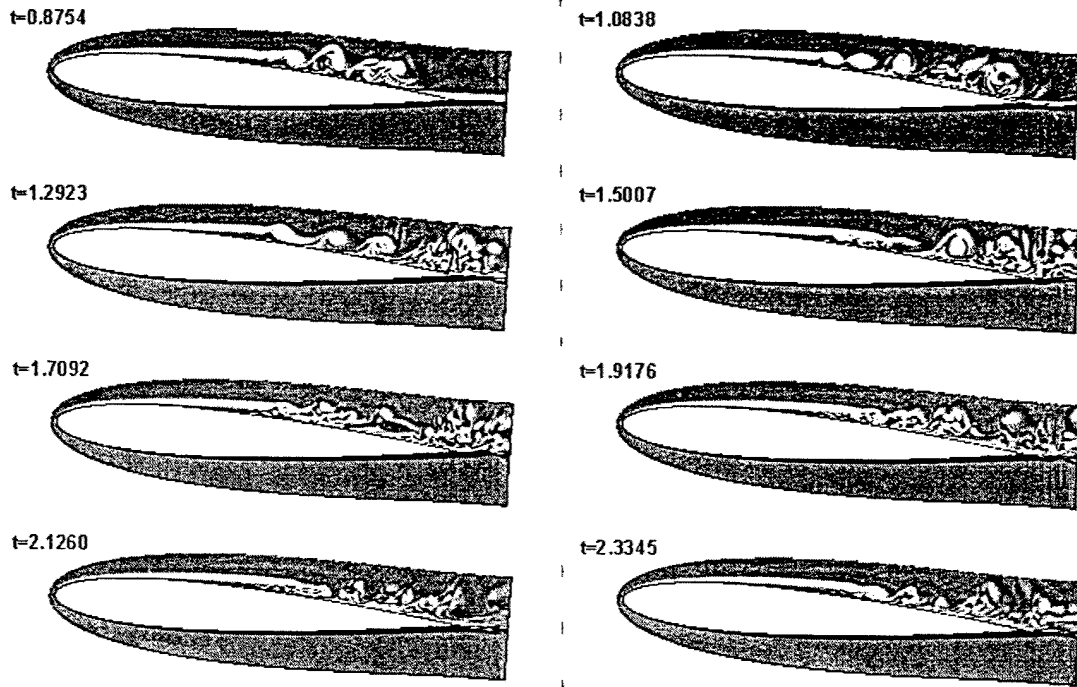
Figure 25. Instantaneous spanwise vorticity at different time

The iso-surfaces of instantaneous vorticity in three directions are plotted in Figure 26. The transition process and breakdown of the rolling-up shear layer are clearly demonstrated in (b). The vortex shed from the separated shear layer are distorted while traveling downstream. The spanwise vorticity iso-surface becomes rippled when 3D vortex appears. Streamwise vortice and wall-normal vortices are shown in (a) and (c) respectively. The interactions of 3D structures cause spanwise vorticity iso-surface to break into small pieces, indicating the breakdown of vortices. The boundary layer becomes fully turbulent after reattaches. During the transition process, the instability wave grows rapidly and is companied by the appearance of the three-dimensional motions which leads to the breakdown of the boundary layer.

(a) streamwise vorticity

(b) spanwise vorticity
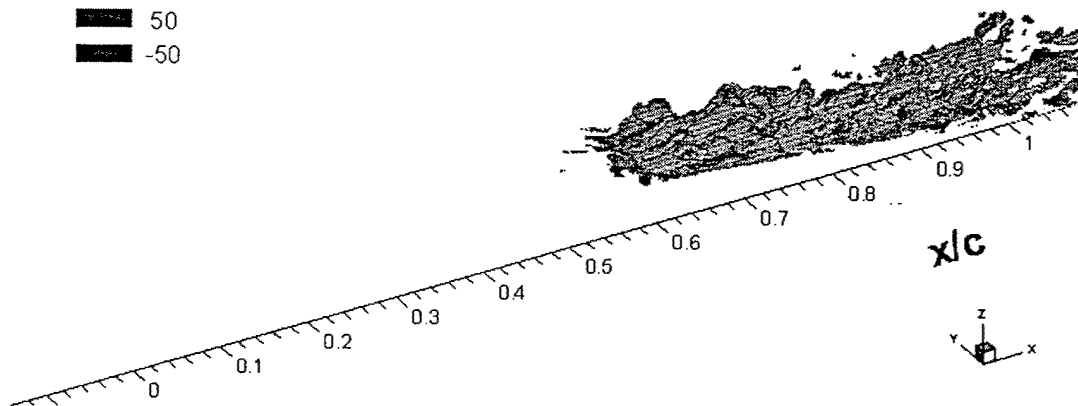
(c) wall-normal vorticity
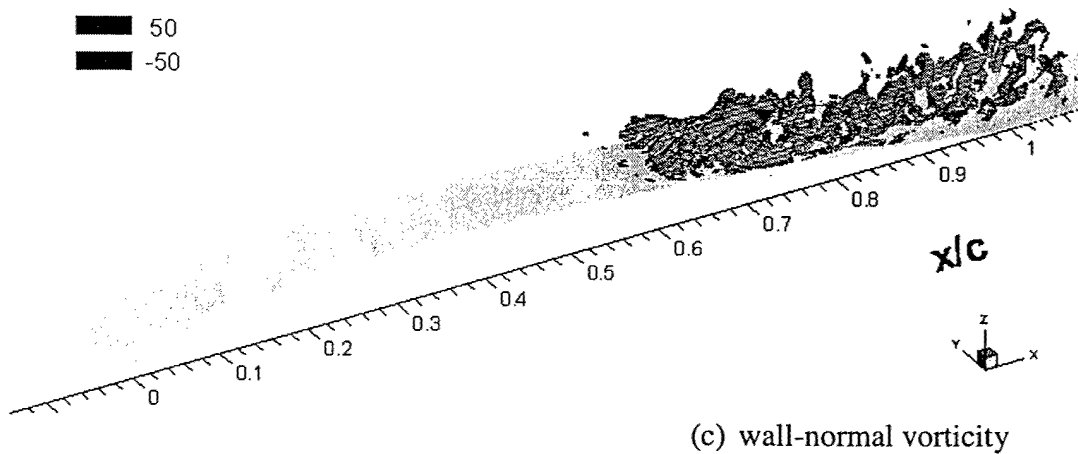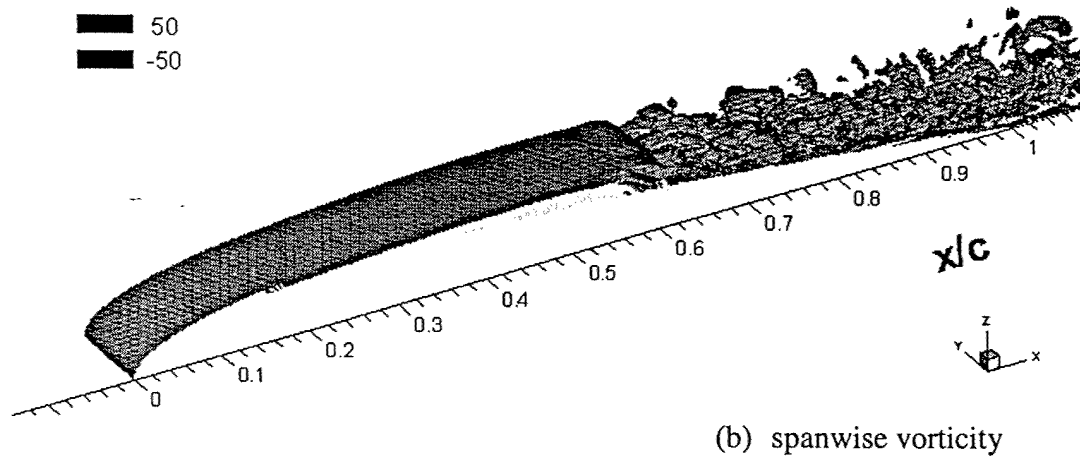
Figure 26. Iso-surface of instantaneous vorticity

From the graphic (Figure 26) and movie made with DNS data, we can find the shed vortex is quickly deformed and stretched. The core of the prime vortex is faded due to dissipation and a negative vortex beside the prime vortex is induced by the prime vortex and, eventually, the prime vortex breaks down to small pieced corresponding to transition to turbulence. From the 3-D graphic (Figure 26), the vortex structure clearly shows the stremwise and spanwise wortex interact and a λ - shape vortex develops, rolls up, and breaks down. From Figure 26, we can find the streamwise vortex plays a key role in the transition process. Whenever the streamwise vortex appears, the vortex rolls up and breaks down quickly. There is a remaining question, where is the stremwise vortex from since there is no 3-D external perturbation added? The possible way could be 3-D acoustic wave from wake (wake instability is 3-D dimensional) or 3-D motion of the shed prime vortex.

Figure 27 shows streamwise evolutions of the vorticity extrema. $\omega_x, \omega_y, \omega_z$ denote vorticity component in streamwise, spanwise and wall-normal directions respectively.

42

The solid lines correspond to maximum values, the dashed lines to minimum values. The streamwise and wall-normal vorticity components remain almost zero up to transition. Downstream, the minimum and maximum vorticity oscillates seriously, showing a symmetrical pattern. The spanwise vorticity component has large value close to the leading edge and remains at a lower level after the separation. Oscillation appears when transition starts.
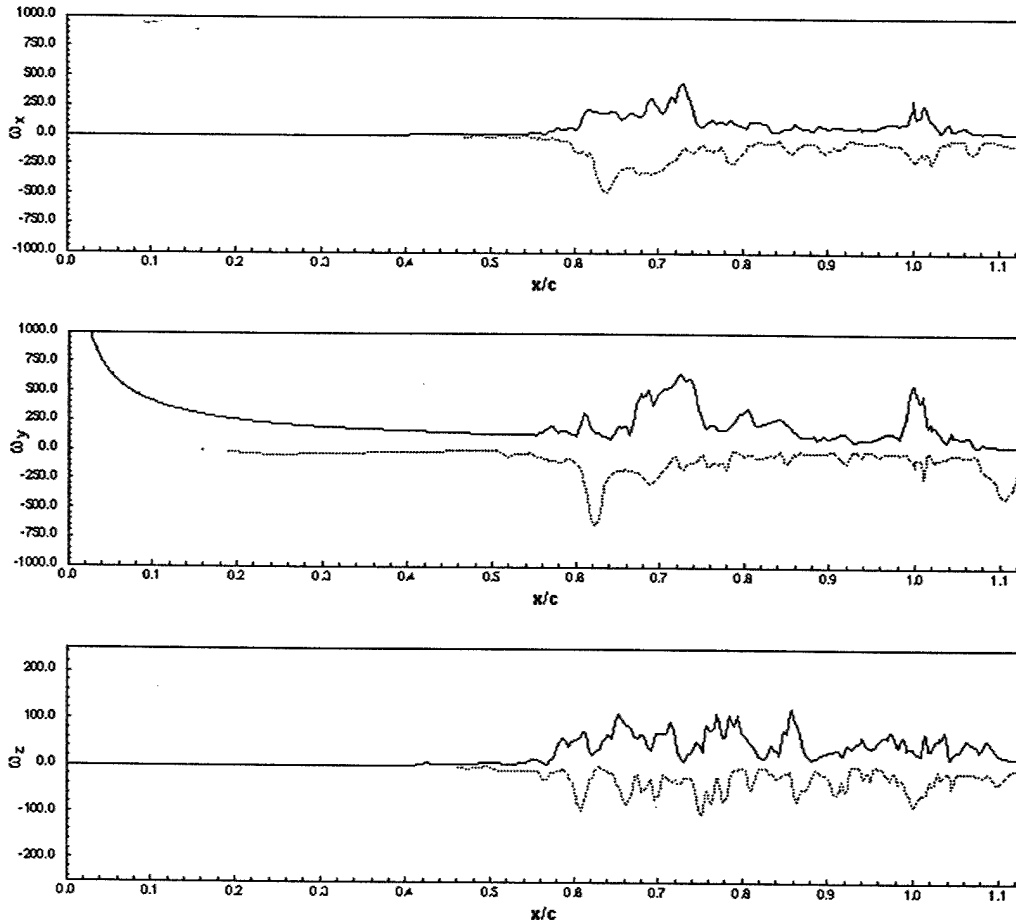

Figure 27 Instantaneous extrema of vorticity

Power spectral density of streamwise velocity at mid-boundary layer is given in Figure 28. Peaks at low frequencies located at $F^+ = 1 \sim 2$, as we discussed in 2D section, correspond to the Kelvin-Helmoltz instability wave and vortex shedding. Stronger peaks at higher frequencies appear gradually further downstream as a result of nonlinear interactions. During and after the transition, energy peaks appear over a wide band of frequency.

43
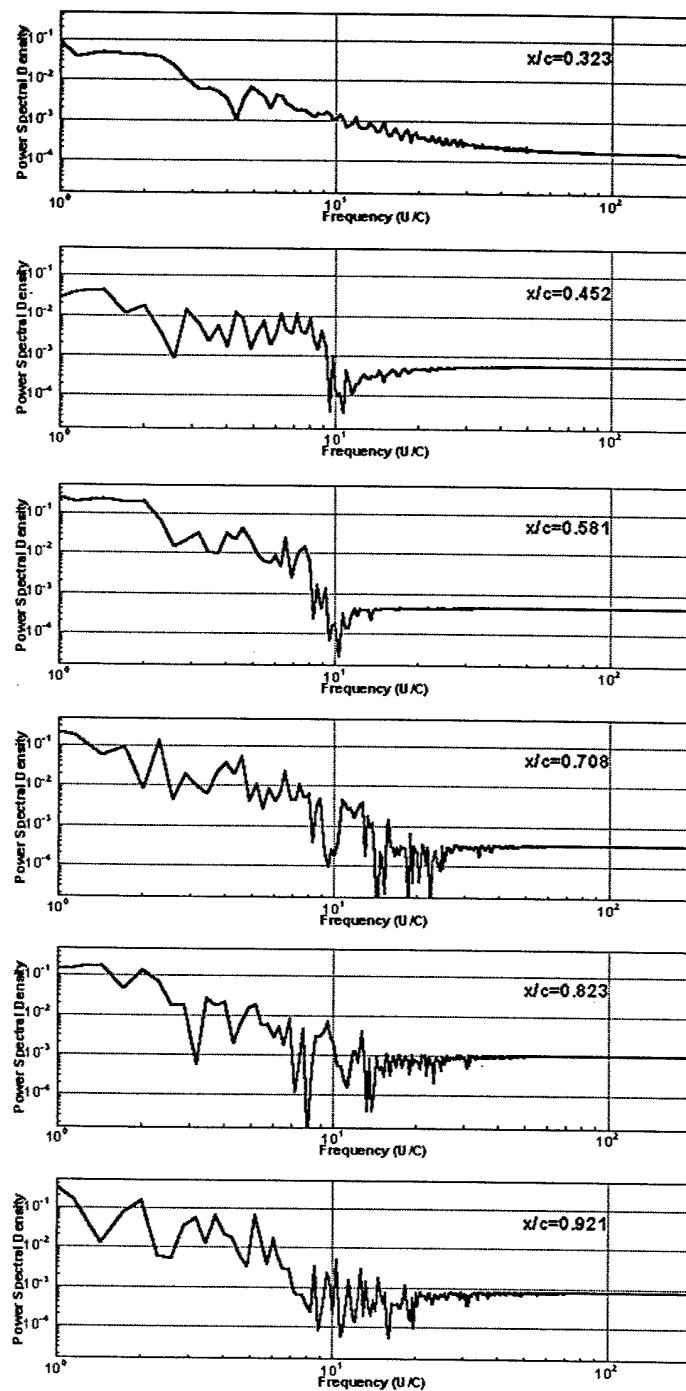
Figure 28. Power spectral density of streamwise velocity

4.5 Conclusion

Separation and transition process on a NACA 0012 airfoil has been investigated by DNS. The following conclusions are drawn based on our observations and results analysis.

The transition to turbulence on an airfoil with attack angle will reattach the separated boundary layer. Though no external disturbances are introduced, the initial perturbations may come from the up-ward traveling acoustic waves generated in the wake. The wake, which is a free shear layer with invicid instability, is most unstable and becomes unstable first. The separation points and the stagnation point are closely related to the pressure distribution on the airfoil surface. The upward traveling acoustic waves may effect the pressure distribution which further changes the location of separation points and stagnation points. This oscillation introduces perturbations inside the boundary layer. The perturbations are convected downstream as vortical disturbances. The separated shear layer has an inviscid instability and the perturbation will be quickly amplified in a rate much higher than the viscous instability. The traveling disturbances trigger the instability waves which are identified as Kelvin-Helmholtz instability. The appearance of 3D motions of the shed prime vortex, where the stremwise vortex appears, and nonlinear interactions of disturbances lead to the sudden growth of disturbances and the generation of high frequencies. The breakdown then happens due to the interaction of spanwise and streamwise vortices. The shed prime vortex is stretched and deformed, the core of the prime vortex is faded, a companion negative vortex is formed, and, eventually, the prime vortex breaks down to small pieces. The shear layer becomes turbulence and reattaches to the surface. This process is then further sustained by the global feed back mechanisms. This analysis leads to the conclusion that reattachment takes place right after the transition, which provides a clue for flow separation control. In order to prevent separation or reduce separation zone, we can use external disturbance to trigger the early transition. When unsteady blowing is used in separation control, the disturbance introduced by unsteady blowing will excite the inherent local instability wave and lead to early transition to turbulence which will reduce the separation zone by early reattachment of the separated shear layer or late separation of the boundary layer. The frequency of the unsteady blowing and the length of the blowing hole provide the frequency and wave length scale for picking up the instability waves. Therefore, the frequency of the pulsed jets should coincide with the frequency of the vortex shedding.

Chapter 5

DNS for Flow Separation Control with Pulsed Jets

The problem set up is same as in Chapter 4, but blowing jets have been added in the forehead of airfoil before the flow separation.

5.1 Results and Analysis

To study the separation and transition processes on the airfoil and the effects of different types of blowing on separation and transition, we set up four cases: I. Baseline case without blowing; II. Pulsed blowing; III. Blowing velocity with 30^0 pitch angle and 90^0 screw angles.

All simulations are carried out with a time step equal to $8.35 \times 10^{-5} C/U_\infty$. The corresponding CFL number is around 400.

5.1.1 Flow around the airfoil without blowing (Baseline Case)

Case I is the baseline case without blowing. 2D solutions are used as the initial field. For this case, the time integration has reached $t = 3.474C/U_\infty$. Mean values are obtained by performing averaging in the spanwise direction and in time over a period of $3C/U_\infty$. The details of the results have been give in Chapter 4

5.1.2 Flow around the airfoil with a pulsed blowing jet

Based on above observations and analysis for baseline case, we set up two cases (actually three cases, but the steady blowing has similar results as the pulsed jet with more mass flow and, therefore, is not reported here) to investigate how the blowing jet (vortex generation jet or VGJ) effects the transition process. All flow parameters and geometry are the same as in baseline case except for that blowing is introduced on suction side of the airfoil. The unsteady blowing is enforced from $x_0 = 0.153$ to $x_1 = 0.175$, which is before the separation point $x_s = 0.19$. The non-dimensional frequency of blowing $F^+ = FC/U_\infty$ is set to be 2 (we now believe 1.4 is a better choice), where C is the chord length and F is the frequency. The blowing velocity has 90^0 pitch angle and 0^0 screw-angle. Pitch angle is defined as the angle the jet makes with the local surface and skew angle is defined as the angle of the projection of the jet on the surface relative to the local free-stream. With this configuration, the blowing velocity is set in the wall-normal direction. The blowing velocity is given as follows,

$$w(x, y, t) = Af(x, y)\exp[-k(\frac{2\tau}{T} - 1)^2]$$

where,

$$f(x, y) = [0.5 - 0.5\cos(\theta_x)][0.5 - 0.5\cos(\theta_y)]$$

$$\theta_x = 2\pi \frac{x - x_0}{x_1 - x_0}, \quad \theta_y = 2\pi \frac{y}{L_y}, \quad \tau = t - nT, \quad T = 1/F^+, \quad A = 0.4, \quad k = 12$$

Shape functions in space and time which are used to define spatial distribution and temporal variation of blowing velocity are depicted in Figure 29. $k = 12$ is used in this case. This parameter can be used to control blowing mass.
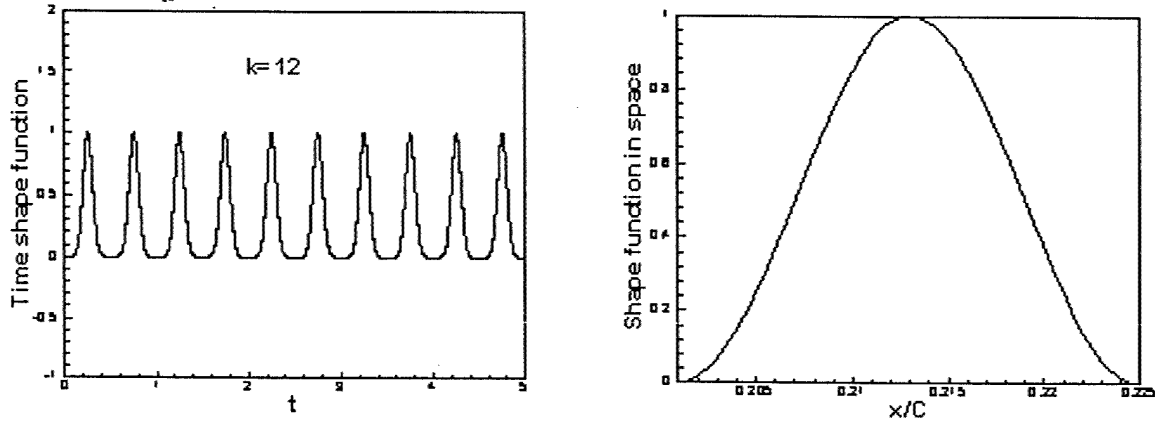

Figure 29. Shape functions in time and space

The time integration for unsteady blowing case has reached $t = 3.73C/U_\infty$. Time averaging is performed over four periods of blowing. Mean velocity vectors are shown in Figure 31a. It is obvious that large separation zone which is clearly seen in the baseline case shown in Figure 17 is dramatically reduced (almost removed). When we look at streamwise mean velocity profiles of baseline case (Figure 17 and Figure 31a) and blowing case which are shown in Figure 31b, we can find that reverse flow completely disappear after $x/c = 0.4$ and boundary layer becomes attached to the surface afterwards.
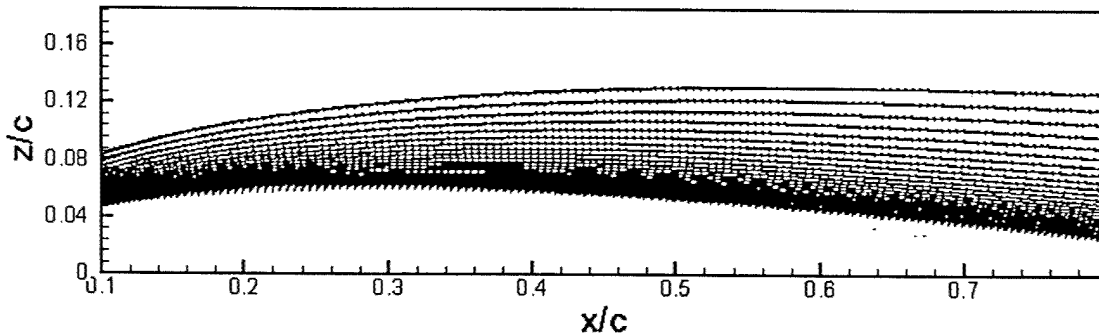
Figure 30. Mean velocity vectors

47
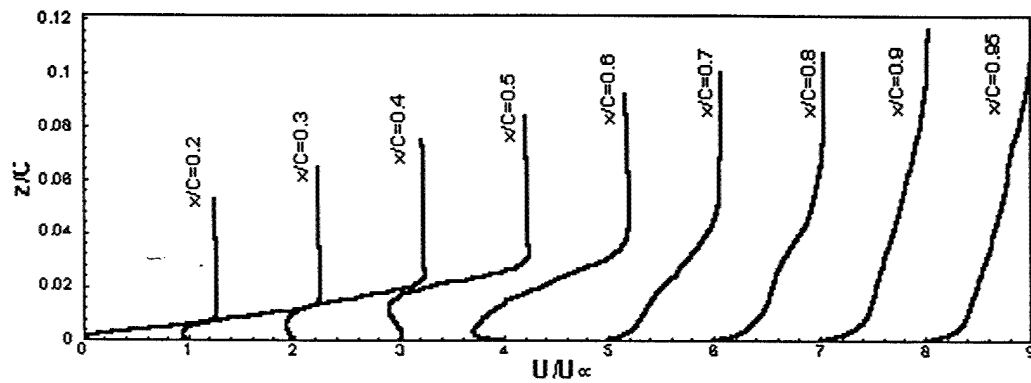
(a) base line case
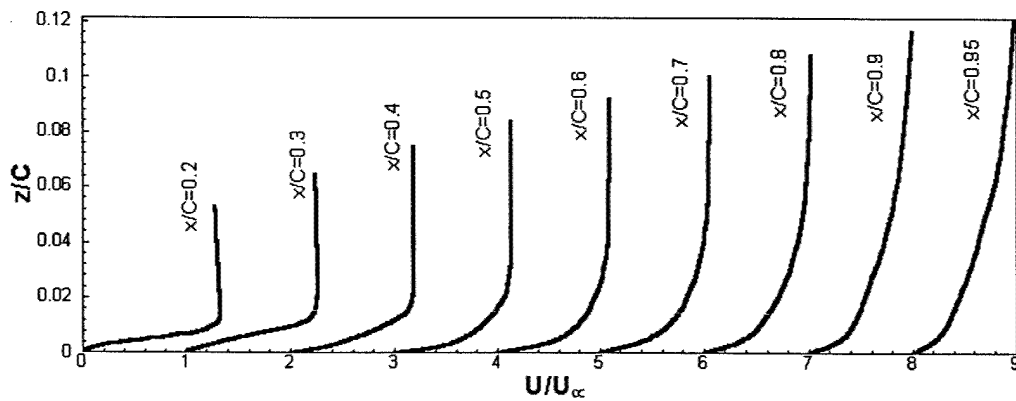
(b) blowing case

Figure 31 Streamwise mean velocity profiles

The reduced separation zone can also been seen from Figure 32 in which the maximum reverse velocity is depicted against streamwise location. Under the effect of blowing, reverse flow happens in very short distance from $x/c = 0.2 \sim 0.3$. Compared with Figure 19, the reverse flow quickly reaches maximum value which is about 7% of free stream velocity. While in the baseline case, the reverse flow velocity gradually increases and reach maximum of about 8% free stream velocity. This difference effects the growth of disturbances which will be discussed later. The distribution of mean pressure coefficient is plotted in Figure 33. As the separation zone is reduced, the flattened area no longer exists. Obviously, this pressure coefficient distribution will not improve the lift force. Temporal variations of lift and drag coefficients which are averaged over spanwise direction are shown in Figure 34. For our case, the reduction of the separation zone decreases both drag and lift forces.
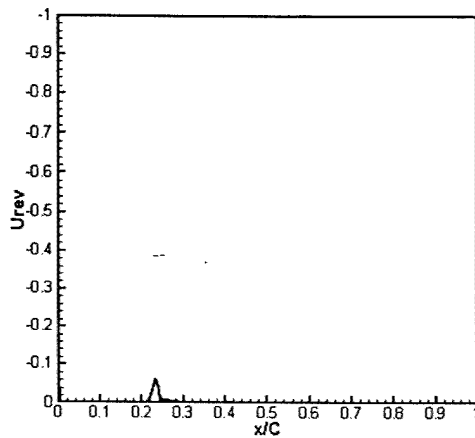
Figure 32. Mean reverse flow distribution on the suction side, $U_{rev} = \min(\overline{u})$
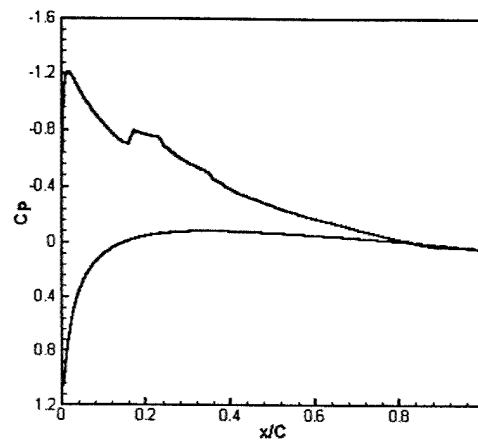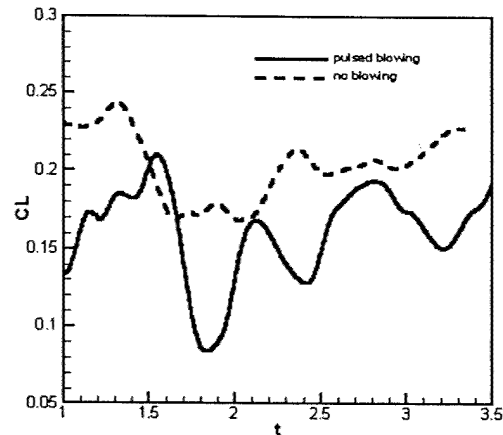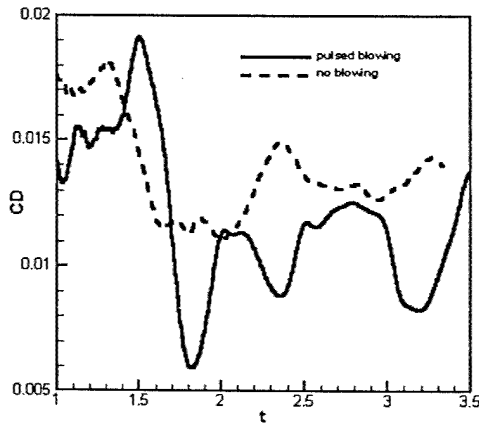
Figure 33. Mean pressure coefficient

Figure 34. Temporal variations of lift and drag coefficients

The skin friction coefficient distribution on the suction side is shown in Figure 35. Figure 36 shows peak r.m.s of velocity fluctuations. In the separation zone, skin friction coefficient is negative. At around $x/c = 0.4$, there is a rapid growth of skin friction, indicating the transition to turbulence. As discussed before, there are disturbances coming from the leading edge. The rapid growth of streamwise and wall normal velocity fluctuations starts after blowing injection point. After a very short distance, they reach a steady level. The growth rate of spanwise velocity is more rapid than in baseline case. The spanwise velocity fluctuation reaches a stable level around the reattachment point $x/c = 0.4$. In this case, transition takes place in very short distance and disturbance level is much lower than in the baseline case. Figure 37 shows the r.m.s streamwise fluctuation velocity profiles at different x locations. Inside the separation zone, from $x/c = 0.2 \sim 0.4$, peak values can be seen inside the boundary layer, indicating the development of the instability waves. After reattachment, this multi-peak profiles no longer exist.
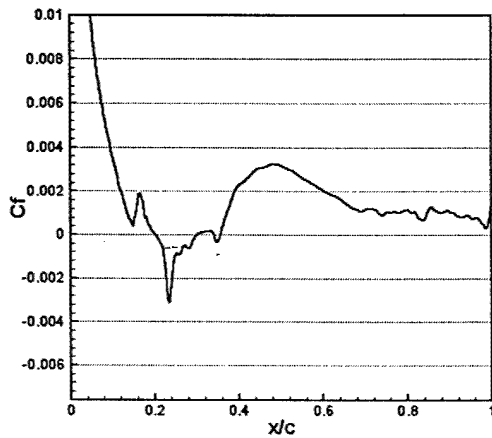
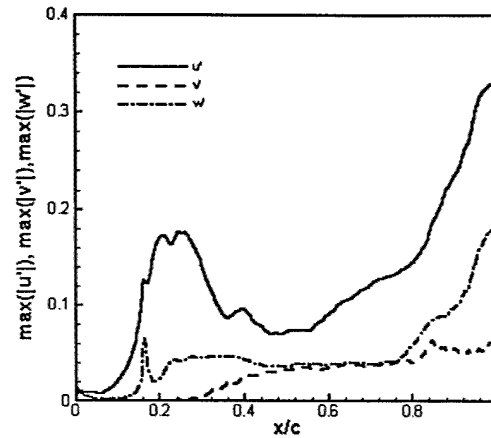Figure 35. Skin friction coefficient distribution on the suction side

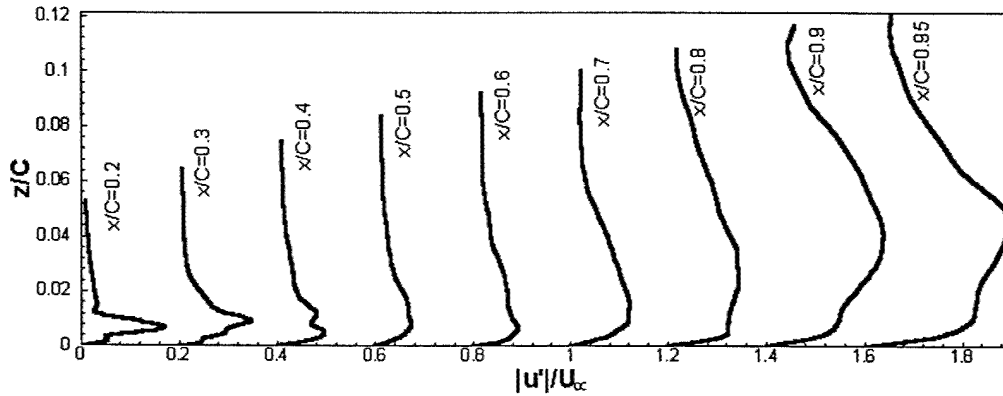Figure 36. Peak r.m.s across the boundary layer

Figure 37. r.m.s streamwise fluctuation velocity profiles

The instantaneous vorticity in spanwise directions at different time are plotted in Figure 38. The simulation is started from 2D solution as the baseline case. At the early stage of simulation, we can see large vortex shedding. The unsteady blowing enforced before the separation point triggers the early transition of the boundary layer. The boundary layer reattaches shortly after separation and form a short separation zone. Reattached boundary layer further becomes fully turbulent. By comparing Figure 25 and Figure 37, the separated shear layer can be clearly seen in Figure 24. In Figure 38 the boundary layer is disturbed by the blowing and transition takes place much earlier than in the non-blowing (baseline) case and the separation zone is significantly reduced.
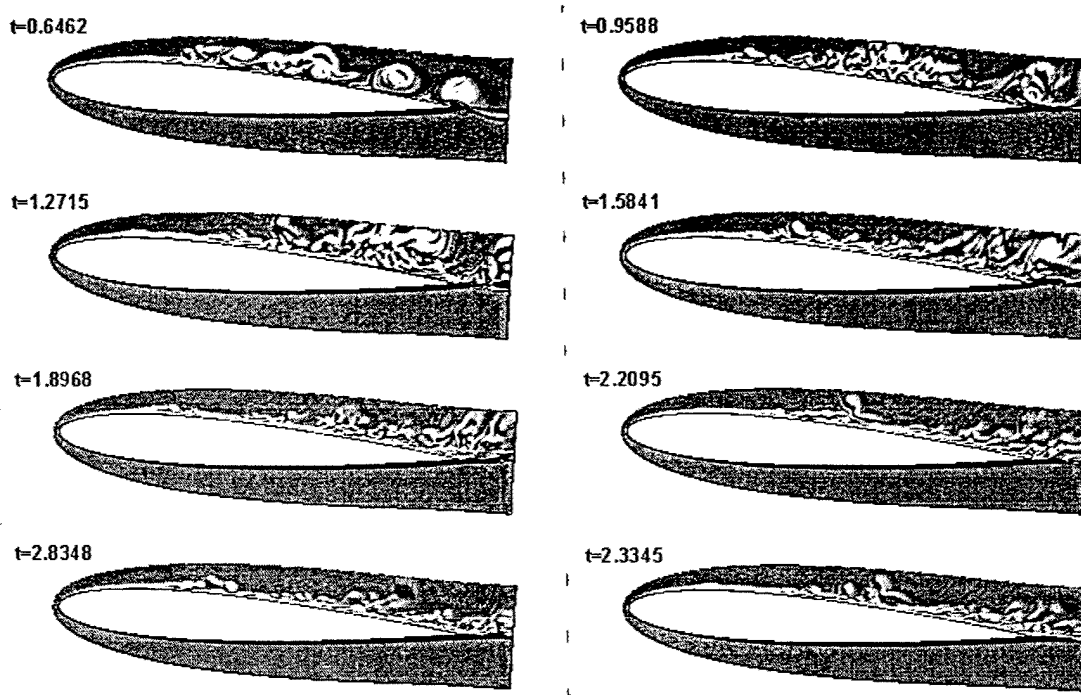
50

t=0.6462 t=0.9588
t=1.2715 t=1.5841
t=1.8968 t=2.2095
t=2.8348 t=2.3345

Figure 38. Instanteneous spanwise vorticity at different time

The iso-surfaces of vorticity components are plotted in Figure 39. The breakdown of the separated shear layer and the development of vortex structure can be clearly seen. Instantaneous extrema of vorticity components are depicted in Figure 40. Compared to Figure 26, in this blowing case, large oscillations of the vorticity components appear much earlier than in the base line case, which indicates the early transition.

(a) streamwise vorticity

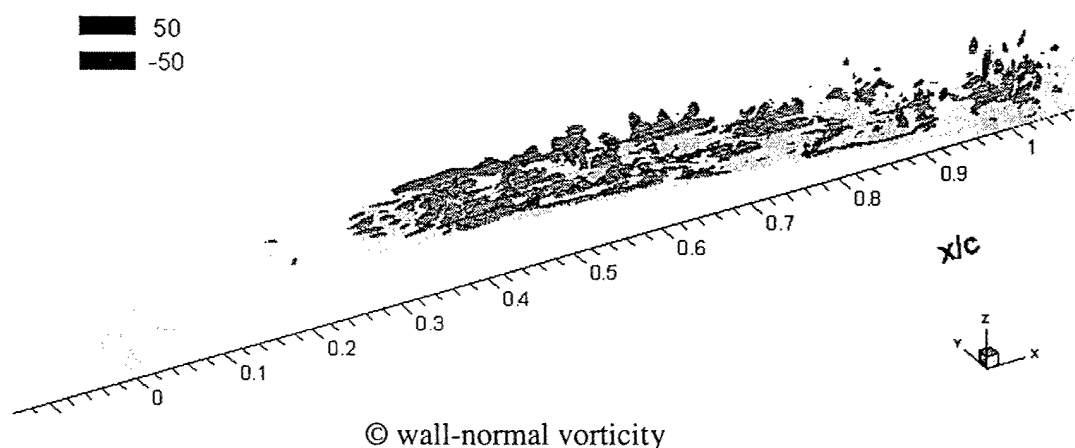(b) spanwise vorticity
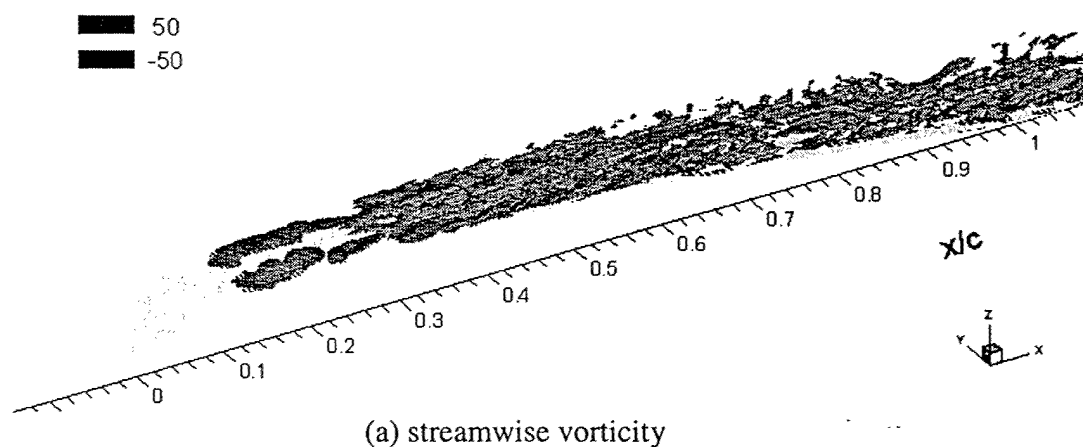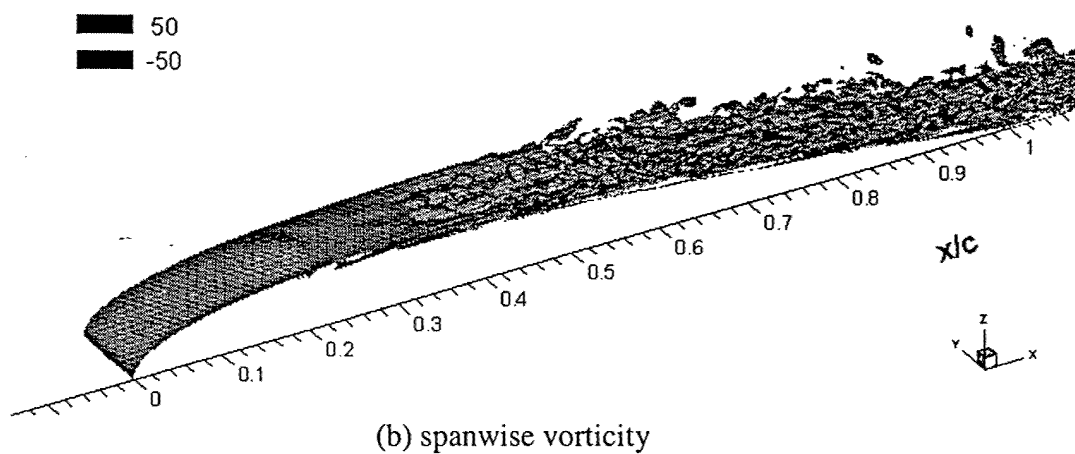

© wall-normal vorticity
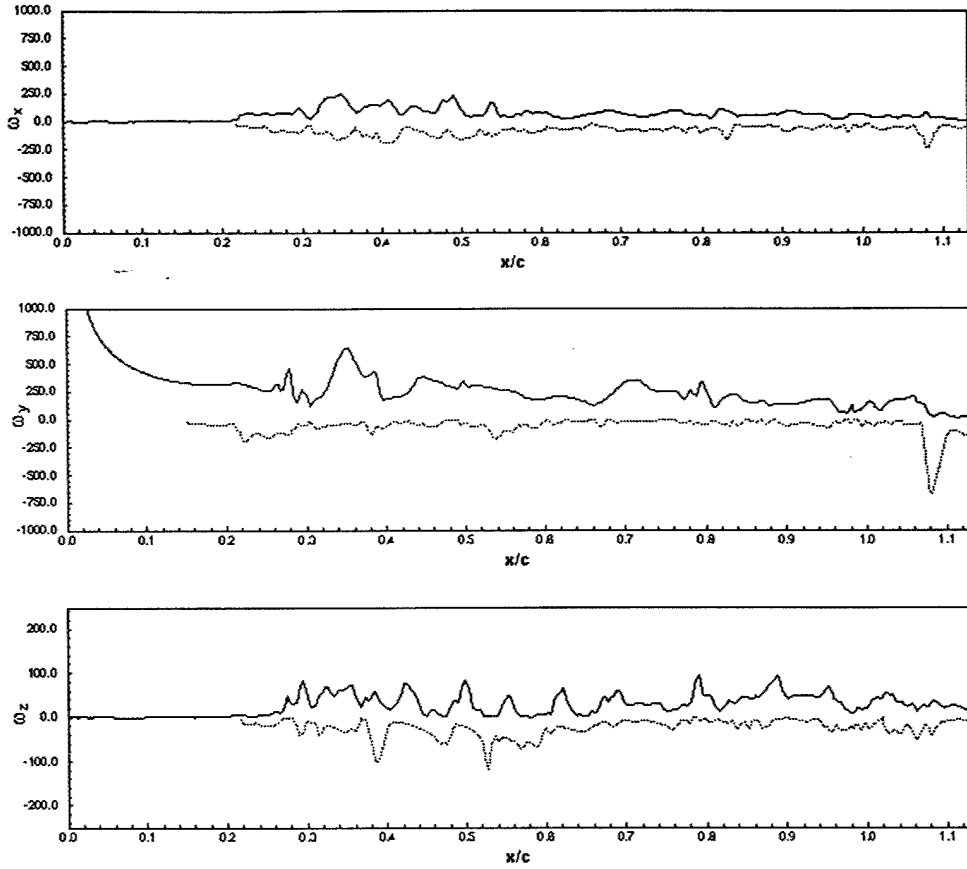Figure 39. Iso-surfaces of vorticity components

Figure 40. Instantaneous extrema of vorticity components

Figure 41 shows the spectrum of the streamwise velocity. Strong peaks at the pulsing frequency $(F^+ = 2)$ and harmonic multiples can be clearly seen at all locations, which mean that the spectrum is dominated by the forcing frequency and its harmonics. Comparing with spectrum in baseline case (Figure 18), high frequency peaks appear earlier than in baseline case, indicating the early transition.
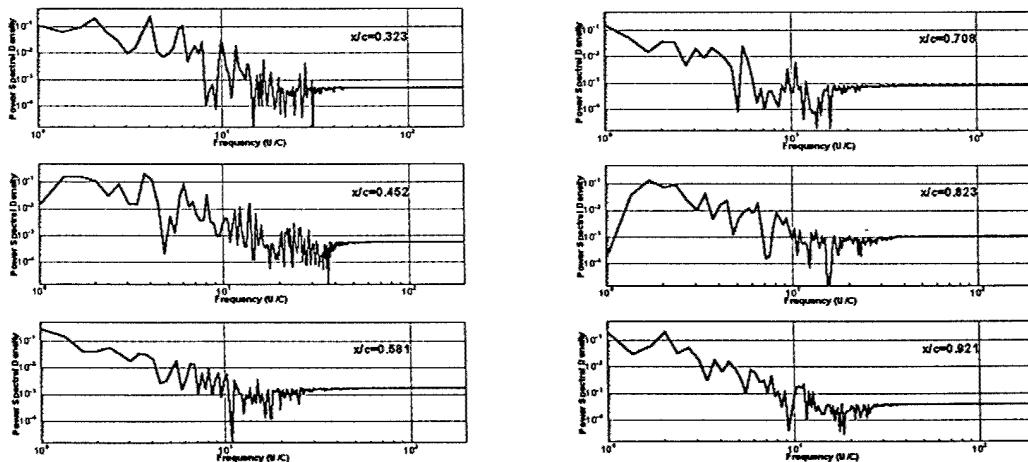

Figure 41. Power Spectral Density of streamwise velocity

From the simulation results and analysis of this pulsed blowing case, we conclude that properly selected unsteady blowing can trigger the early transition through exciting most unstable waves and non-linear interactions. In this case, we didn't observe the unstable mode picking up mechanism, because transition takes place in very short distance. This may be due to the large blowing mass flow which introduces a very large disturbance and leads to bypass transition. To discover the unstable mode pick up mechanism, future selection of blowing jets should be with small blowing mass flow (very sharp shape in time with large k) and with a near vortex shedding frequency. Though the separation zone is reduced, both lift and drag are decreased. This shows that the increase of the ratio of lift over drag can happen for large attack angle, but not for small attack angles (4° for example in our case) although the separation is almost completely removed. Large attack angles for low Reynolds number flow may be selected as a target for future study of flow separation control where the ratio of lift over drag should be significantly improved.

5.1.3 The effect of blowing angle

To study the effect of blowing angle, we setup another case to simulate flow around the airfoil with pulsed blowing of 30^0 pitch angle and 90^0 screw angle. The flow parameters and geometry are the same as the second case, except the blowing velocity has a pitch angle of 30^0. The vectors of blowing velocity are shown in Figure 42. The profile of the blowing velocity in streamwise and spanwise directions are also shown in Figure 42. One injection hole is centered at $y/c = 0.05$.
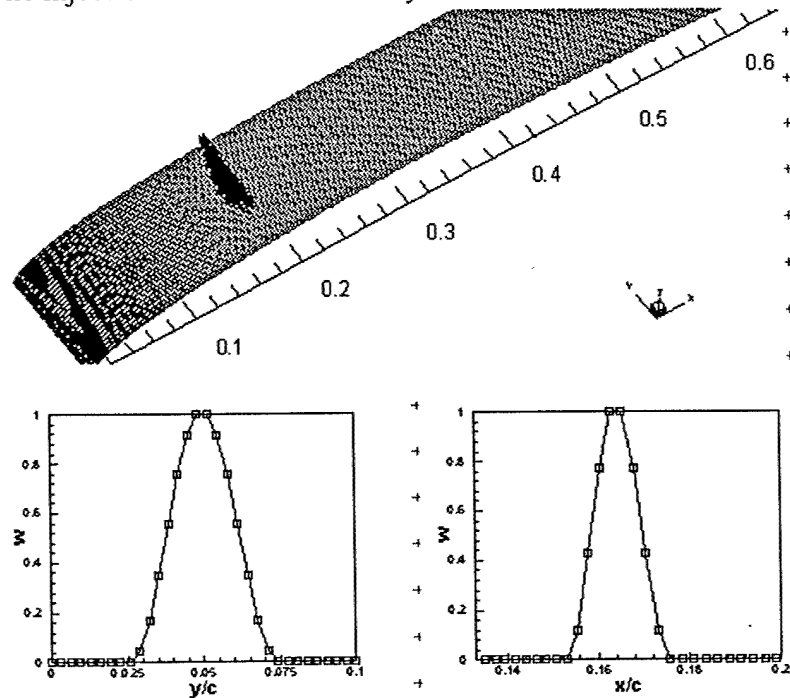

Figure 42. Distribution of blowing velocity

As the time integration is not long enough for statistic analysis, we only present some instantaneous results here. More detailed analysis and comparison with the normal blowing case will be given in the future paper or reports.

This simulation was started from the solution of the baseline case at $t = 2.33C/U_\infty$. Figure 43 shows the evolution of instantaneous spanwise vorticity. At the initial stage, the separation zone can be clearly identified. When disturbances introduced by the blowing enter the separated shear layer, disturbances are amplified when traveling downstream. At $t = 0.6253C/U_\infty$, we can see the rippling of the shear layer and the vortex shedding after the rippling. At later stage, the separation zone totally disappeared.

t=0.2084   t=0.4196

t=0.6253   t=0.8338

t=1.0922   t=1.2506
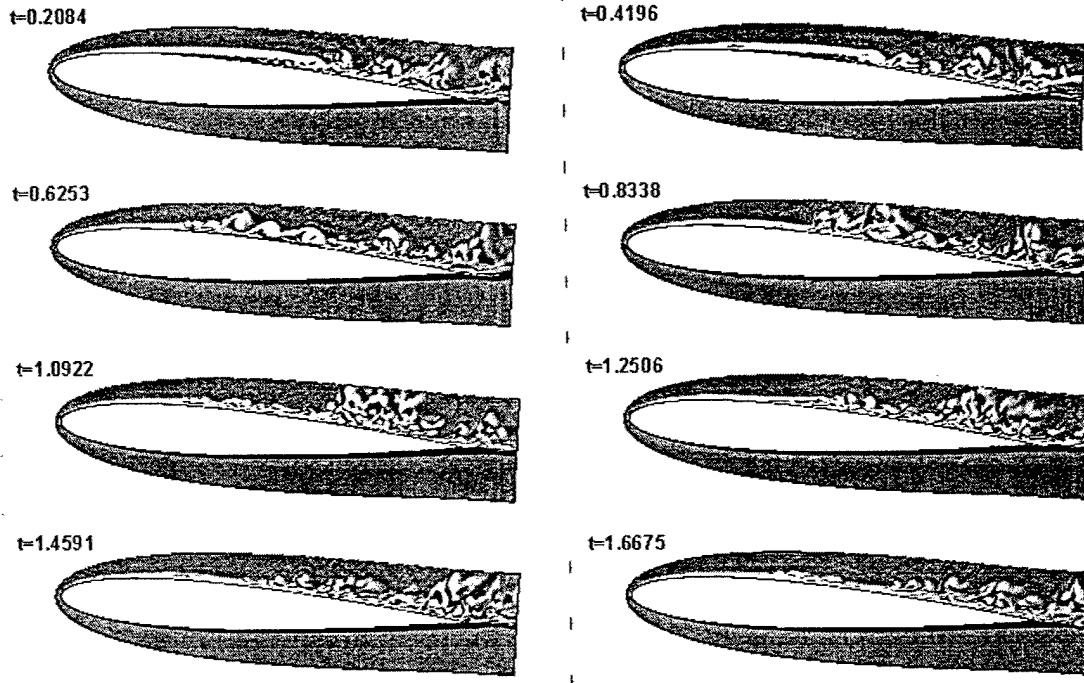
t=1.4591   t=1.6675

Figure 43 Instantaneous spanwise vorticity at different time

Figure 44 shows the iso-surface of instantaneous vorticity components at $t = 1.776C/U_\infty$. Although the experiment (Bons et al, 2001) shows the pitched jet will obtain a better efficiency due to the un-symmetric vortex structure, no much difference from the normal blowing case was found at this simulation stage. This may be caused by the large blowing mass flow in both cases where the unstable mode pick up mechanism is not found, but bypass transition occurs. The other reason is the length of integration in time is not long enough for the statistic analysis. More time integration is needed for the pitched jet case.
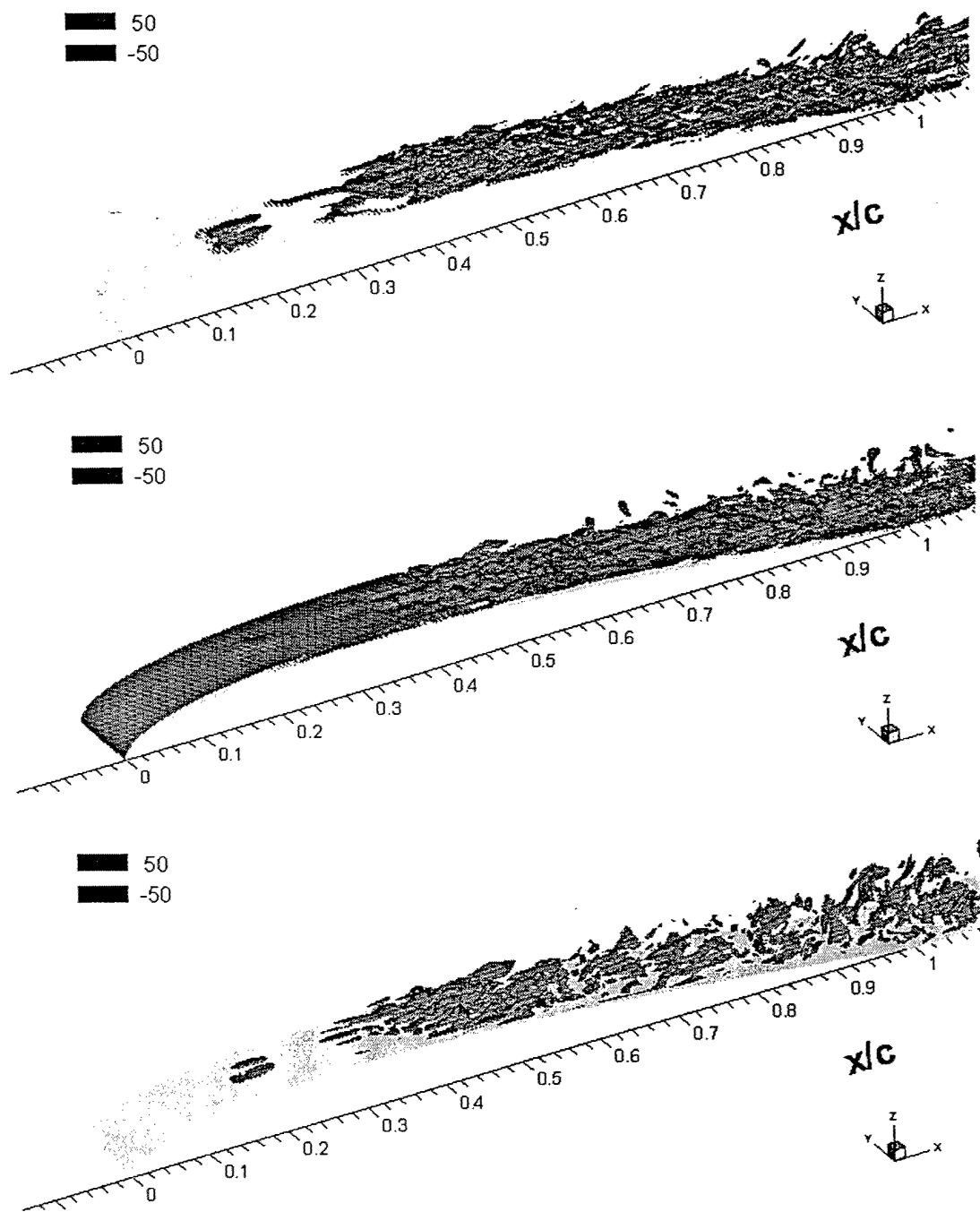
Figure 44. Iso-surface of vorticity components

5.2 Conclusion

Separation and transition processes on a NACA 0012 airfoil with or without jet blowing on the surface have been investigated. The following conclusions are drawn based on our observations and results analysis.

56

Properly selected unsteady blowing can trigger the early transition through exciting most unstable waves and non-linear interactions. In our cases, we didn't observe the unstable mode picking up mechanism, because transition takes place in very short distance. This may be caused by the large mass flow of the blowing jets which cause the bypass transition. Though the separation zone is reduced, both lift and drag are decreased. Future work should select the large attack angle, small mass flow with large k in blowing jets, and appropriate blowing frequencies corresponding to vortex shedding frequency which is around $F^+ = 1.4$ in our case.

The DNS data have been post-processed as a movie which can be obtained by sending a request to Dr. Chaoqun Liu at cliu@uta.edu.

Acknowledgment

References

[1] AGARD-CP-551, {Application of direct and large eddy simulation to transition and turbulence}, 74th Fluid Dynamics Symposium held at Chania, Crete, Greece, April, 1994.

[2] Adams, N. A. "Direct simulation of the turbulent boundary layer along a compression ramp at M=3 and $R_{e\theta} = 1685$", J. of Fluid Mechanics, Vol. 420, pp. 47-83, 2000

[3] Bertolotti, F. P., Herbert, T., Spallart, P. R., "Linear and nonlinear stability of the Blasius boundary layer", *Journal of Fluid Mechanics*, Vol. 242, pp441-474, 1992.

[4] Boiko, A. V., Grek, G. R., Dovgal, A. V., Kozlov, V. V., "The origin of turbulence in near-wall flows", pp 167-196, *Springer*, 2002.

[5] Bons, J. P., Sondergarrd, R., and Rivir, R. B., "Turbine Separation Control Using Pulsed Vortex Generator Jets", *Journal of Turbomachinery*, Vol.123, pp.198-206, 2001.

[7] Drazin, P. G., Reid, W. H., "Hydrodynamic Stability", pp1-50, *Cambridge University Press*, 1981.

[8] Choudhari, M., Chang, C.L., Jiang, L., Liu, C., Direct Numerical Simulation of Instability-Wave Generation and Propagation in Supersonic Boundary Layers, The 2003 International Conference on Computational Science and Its Applications (ICCSA 2003), Montreal, Canada, May 18 - May 21, 2003, Springer-Verlag Lecture Notes in Computer Science volume.

[9] Choudhari, M., Chang, C.L., Jiang, L., Liu, C., Cross-validation of DNS and PSE results for instability-wave propagation in compressible boundary layers past curvilinear surface, submitted to AIAA CFD Conference, Orlando, Florida, June 2003.

[10] Ducros, F., Comte, P. and Lesieur, M., Large-eddy simulation of transition to turbulence in a boundary layer developing spatially over a flat plate, J. Fluid Mech. 326, pp.1—36, 1996.

[11] Harten, A., et al, Uniformly high order accurate essentially non-oscillatory scheme, III, J. Comput. Phys., 71, pp.231-303, 1987.

[12] Lele, S. K., Compact finite difference schemes with spectral-like resolution, Journal of Computational Physics, Vol.103, pp.16-42, 1992.

[13] Jiang, G. S., Shu, C. W., Efficient implementation of weighted ENO scheme. J. Comput. Phys., 126, pp.202—228, 1996.

[14] Jiang, L. Shan, H., and Liu, C., Direct numerical simulation of boundary-layer receptivity for subsonic flow around airfoil. Recent Advances in DNS and LES,

Proceedings of the Second AFOSR (Air Force Office of Scientific Research) International Conference. Rutgers, New Jersey, June 7-9, 1999a.

[15] Jiang, L. Shan, H., Liu, C., and Visbal, M., Non-reflecting boundary conditions for DNS in curvilinear coordinates. Recent Advances in DNS and LES, Proceedings of the Second AFOSR (Air Force Office of Scientific Research) International Conference. Rutgers, New Jersey, June 7-9, 1999b.

[16] Jiang, L., Shan, H., and Liu, C., Weighted Compact Scheme for Shock Capturing, International Journal of Computational Fluid Dynamics, Vol. 15, pp. 147-155, 2001a.

[17] Jiang, L. and Liu, C., "Direct numerical simulation for flow transition validation", NASA Langley Report, 2001b.

[18] Jiang, L. and Liu, C., Direct numerical simulation for flow separation control with pulsed jets, AIAA Paper 2003-0611, Reno, 2003.

[19] Liu, Z., Liu, C., and McCormick, S., Multilevel adaptive methods for incompressible flow in grooved channels, J.of Computational and Applied Mathematics, vol. 38, pp. 283-295, 1991a.

[20] Liu, Z., Liu, C., and McCormick, S., Multigrid methods for flow transition in a planar channel, Computer Physics Communications, 65, pp. 188-200, 1991b.

[21] Liu, Z. and Liu, C., High order finite difference and multigrid methods for spatially-evolving instability, Journal of Computational Physics, Vol 106, pp. 92-100, 1993.

[22] Liu, Z. X., Liu, C., and McCormick, S., Multilevel methods for temporal and spatial flow transition simulation in a rough channel, International Journal for Numerical Methods in Fluids, Vol 18, 1994a.

[23] Liu, Z. and Liu C., Fourth order finite difference and multigrid methods for modeling instability in flat plate boundary layers - 2-D and 3-D approaches, J. Computers and Fluids, Vol 23, No.7, pp. 995-982, 1994b.

[24] Liu, C. and Liu, Z., Multigrid mapping and box relaxation for simulation of the whole process of flow transition in 3-D boundary layers, J. of Computational Physics, Vol 119, pp. 325-341, 1995.

[25] Liu, Z., Xong, G., and Liu, C., A contravarient velocity based implicit multilevel method for simulating the whole process of incompressible flow transition around Joukowsky airfoils, J. of Applied Mechanics and Engineering, pp111-161, No. 1, Vol. 3, 1998a.

[26] Liu, C., Multigrid Methods for Steady and Time-Dependent Flow, Invited Review Paper, Computational Fluid Dynamics Review, Vol. 1, pp512-535, Edited by Hafez and Oshima, 1998b.

[27] Liu, X. D., Osher, S., Chan, T., Weighted essentially non-oscillatory schemes, J. Comput. Phys., 115, pp.200-212, 1994.

[28] Masad, J. A., Iyer, V., "Transition prediction and control in subsonic flow over a hump", *Phys. Fluids*, 6 (1), pp313-327, 1994

[29] Normand, X. and Lesieur, M., Direct and large-eddy simulation of transition in compressible boundary layer, Theoret. Comput. Fluid Dyn., 3, pp231-252, 1992.

[30] Pacheco, P.S., Parallel Programming with MPI, Morgan Kaufmann Publishers, Inc. 1994.

[31] Rizzetta, D. P. and Visbal, M. R. "Large–eddy simulation of supersonic compression-ramp flows" AIAA 2001-2858, June 11-14, 2001.

[32] Shan, H., Jiang, L., and Liu, C., Large eddy simulation of flow transition in a compressible flat-plate boundary layer at Mach number 4.5, International Journal of Computational Fluid Dynamics, Vol. 13, pp25-41, 1999a.

[33] Shan, H., Jiang, L., and Liu, C., Direct numerical simulation of leading edge receptivity in a flat-plate boundary layer, International Journal of Computional Fuild Dynamics, Vol 3, pp470-480, 1999b.

[34] Shan, H., Jiang, L., and Liu, C. Study of flow transition in a supersonic flat-plate boundary layer: Large eddy simulation and validation, International Journal of Computational Fluid Dynamics, Vol 8, pp208-219, 1999c.

[35] Shan, H., Jiang, L., and Liu, C., Direct numerical simulation of three-dimensional flow around a delta wing. AIAA Paper 2000-0402. The 38th AIAA Aerospace Sciences Meeting and Exhibit, Reno, NV, January 10-13, 2000a.

[36] Shan, H., Jaing. L., and Liu, C., Numerical Investigation of Compressible Separated Flow around a NACA 0012 Airfoil at 12 Degree Angle of Attack, International Journal of Computational Fluid Dynamics , Vol. 9, No. 2, pp84-92, 2000b.

[37] Shan, H., Jiang, L., and Liu, C., Numerical simulation of complex flow around a 85 delta wing. Proceedings of the Third AFOSR (Air Force Office of Scientific Office) International Conference on DNS/LES. Arlington, Texas, August 5-9, 2001.

[38] Street, C. L., and Macaraeg, M. G., Spectral multi-domain for large-scale fluid dynamics simulations, Appl. Num. Math., 6, pp.123, 1989.

[39] Shu, C. W., Osher, S., Efficient implementation of essentially non-oscillatory shock-capturing schemes , J. Comput. Phys.,77, pp.439-471, 1988.

[40] Shu, C. W., Osher, S., Efficient implementation of essentially non-oscillatory shock-capturing schemes II, J. Comput. Phys.,83, pp.32-78, 1989.

[41] Spekreijse, S.P., Elliptic grid generation based on Laplace equations and algebraic transformation, J. Comp. Phys., Vol. 118, pp.38—61, 1995.

[42] Thompson, K. W., Time dependent boundary conditions for hyperbolic systems, I, J. Comput. Phys., 68, pp.1—24, 1987.

[43] Thompson, K. W., Time dependent boundary conditions for hyperbolic systems, I, J. Comput. Phys., 89, pp.439—461, 1990.

[44] Visbal, M. R. and Gaitonde, D. V., High-order accurate methods for unsteady vortical flows on curvilinear meshes, AIAA Paper 98-013, 1998.

[45] Yang, Z.Y., Voke, P.R., "Large-eddy simulation of boundary-layer separation and transition at a change of surface curvature", *Journal of Fluid Mechanics.* Vol.439, pp.305-333, 2001.

[46] Yoon, S., Kwak D., Implicit Navier-Stokes solver for three-dimensional compressible flows, AIAA Journal, 30, pp.2653-2659, 1992.